A. P. Alexandrov
RESEARCH INSTITUTE
OF TECHNOLOGY
NITI

Investigation of corium melt interaction with NPP reactor vessel steel

(METCOR-P)

PROGRESS REPORT

01/07/09 –31/12/09

INTERACTION OF MOLTEN CORIUM WITH THE EUROPEAN VESSEL STEEL IN THE OXIDIZING ATMOSPHERE

MCP-4/09 TEST

Project title	Investigation of Corium Melt Interaction with NPP Reactor Vessel Steel (METCOR-P) No. 3592
Contracting organization	ISTC
File code	RMP-04
Project location	FGUP A.P. Alexandrov Research Institute of Technology (NITI) of the Russian Federal Agency for Nuclear Energy. NITI, Sosnovy Bor, 188540 Leningrad Region, Russia

Project manager	Name	V.B. Khabensky
	Signature	
	Date	December 2009

Dr.(Eng.), Prof.	V. B. Khabensky
Dr.(Eng.)	S. V. Bechta
Ph.D.	V. S. Granovsky
Ph.D.	A.A. Sulatsky
Ph.D.	S.A. Vitol
	E.V. Krushinov
Ph.D.	S.Yu. Kotova

Prof., As. Mem, RAS.	V.V. Gusarov
Ph.D.	I. V. Kulagin
Ph.D.	D. B. Lopukh

V. I. Almjashev

V. G. Bliznyuk

V. R. Bulygin

E. K. Kalyago

N. E. Kamensky

A. V. Lysenko

A. P. Martynov

V. V. Martynov

E. V. Shevchenko

A. A. Chertkov

ABSTRACT

The report presents a description and main results of MCP-4 test of the ISTC METCOR-P Project No. 3592.

Kinetics of molten UO_{2+x}-ZrO_2 and UO_{2+x}-ZrO_2-FeO_y coriums interaction with a European reactor vessel steel specimen was studied in air.

CONTENTS

INTRODUCTION

The projects METCOR and METCOR-P encompassed an investigation of molten corium interaction with the cooled vessel steel of Russian reactors in the oxidizing atmosphere. The obtained experimental data were generalized by the proposed corrosion process model. The corrosion kinetics were found to be influenced by corium composition, while the influence of the above-melt atmosphere (steam, air) was insignificant. The obtained results are presented in [1, 2].

In accordance with the METCOR-P Work Plan, MCP-4 test has been carried out in order to determined kinetics of the European vessel steel corrosion in air above the melt. In order to obtain more data, said steel was subjected to interaction with both refractory (UO_{2+x}-ZrO_2) and fusible (UO_{2+x}-ZrO_2-FeO_y) molten coriums within the framework of one test.

The report presents a description of MCP-4 test, its results and their analysis.

1 TEST DESCRIPTION

1.1 Experimental facility diagram

The test was carried out on the Rasplav-3 experimental facility. Diagram of the furnace is shown in Fig. 1.1. The vessel steel specimen is presented in Fig. 1.2. In order to evaluate heat fluxes from melt to the specimen and for cooling the zone of coupling the ultrasonic sensor with the specimen, two calorimeters, the top and bottom ones, were provided.

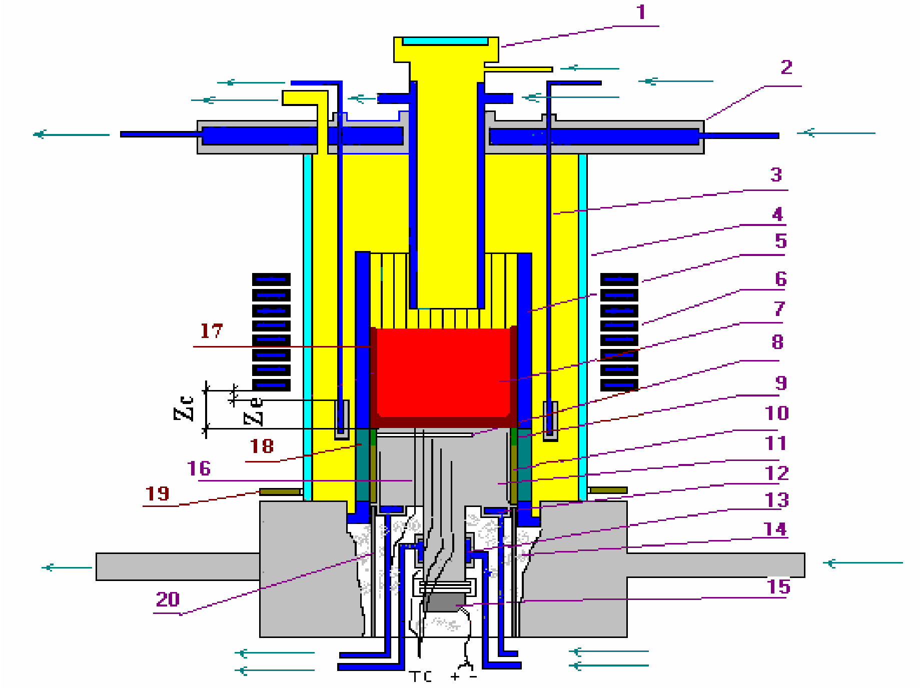

1 – water-cooled pyrometer shaft; 2 – water-cooled cover; 3 – water-cooled electromagnetic screen; 4- quartz tube; 5 – crucible section; 6 – inductor; 7 – melt; 8 – acoustic defect; 9 – molten ZrO_2 (fianite); 10 – powdered ZrO_2; 11 – vessel steel specimen; 12 – top specimen calorimeter; 13 – bottom specimen calorimeter; 14 – mullite wool thermal insulation; 15 – ultrasonic sensor (USS); 16 – K-type thermocouples; 17 – crust, 18 – electromagnetic screen (crucible sections welded together); 19 – uncooled electromagnetic screen; 20 – specimen cylindrical support

Fig. 1.1 – Furnace diagram

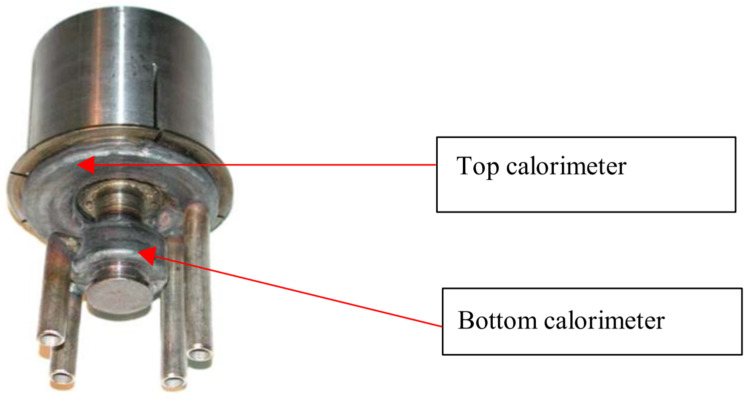

Fig. 1.2 – Vessel steel specimen

Fig. 1.3 and Tab. 1.1 give the locations of K-type thermocouple junctions in the specimen. Within a 10 mm radius from the specimen axis, the thermocouples were embedded into channels Ø 1.5 mm, and within a 29 mm radius – into the 1.5 mm-wide carved grooves.

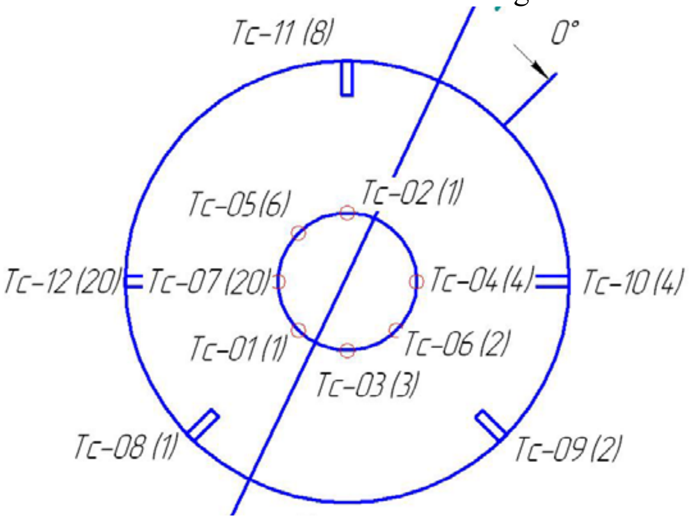

Fig. 1.3 – Thermocouple hot junction locations

Table 1.1 – Coordinates of thermocouple hot junction locations in the specimen

Thermo couple No.	**α° (azimuth angle)**	**r, mm (distance from the specimen axis to the hot junction)**	**h, mm (distance from the melt-facing top to the hot junction)**
Tc-01	180	10	1
Tc-02	315	10	1
Tc-03	135	10	3
Tc-04	45	10	4
Tc-05	270	10	6
Tc-06	90	10	2
Tc-07	225	10	20
Tc-08	180	29	1
Tc-09	90	29	2
Tc-10	45	29	4
Tc-11	315	29	8
Tc-12	225	29	20
USS	45	7.5	104

To exclude electromagnetic heating of the specimen, the lower parts of crucible sections were welded together, and this arrangement served as an electromagnetic screen (18). The specimen was positioned in the crucible so that its top was 1 mm below the welded sections top. The gap between the specimen and crucible sections was filled with ZrO_2 powder (10) and pellets of molten stabilized ZrO_2 (9). An additional screening of specimen from induction heating and the bottom crust thickness control in the molten pool were performed by using a water-cooled movable screen (3). The air-blasted water-cooled pyrometer shaft (1) was used for the melt surface monitoring.

The rate of vessel steel corrosion was determined by ultrasonic sounding. To increase accuracy of this method, an acoustic defect (8) was made in the specimen and the same ultrasonic converter (15) as the one used in tests of the MC series was employed.

In order to make a mass balance for the test, a system for air supply/evacuation has been assembled. Its diagram is presented in Fig. 1.4. The air flow through the furnace was ensured by the vacuum pump (5). A silica gel column (1) for removing moisture from air was installed at the furnace inlet. To clean gases from aerosols, the cyclone (3) and the switched in turn Large Area Filters (4) were employed. To control the gas flow parameters (flow rate, pressure and temperature), electromechanical flow meters G1, G2 of the OP-40/C type, Motorola pressure transducers P1, 2, 3 and L-type thermocouples were installed in places marked by dots in the diagram. The content of oxygen in the supplied air and removed furnace gases was controlled by OXIC electrochemical oxygen sensors (Ox_2, Ox_1).

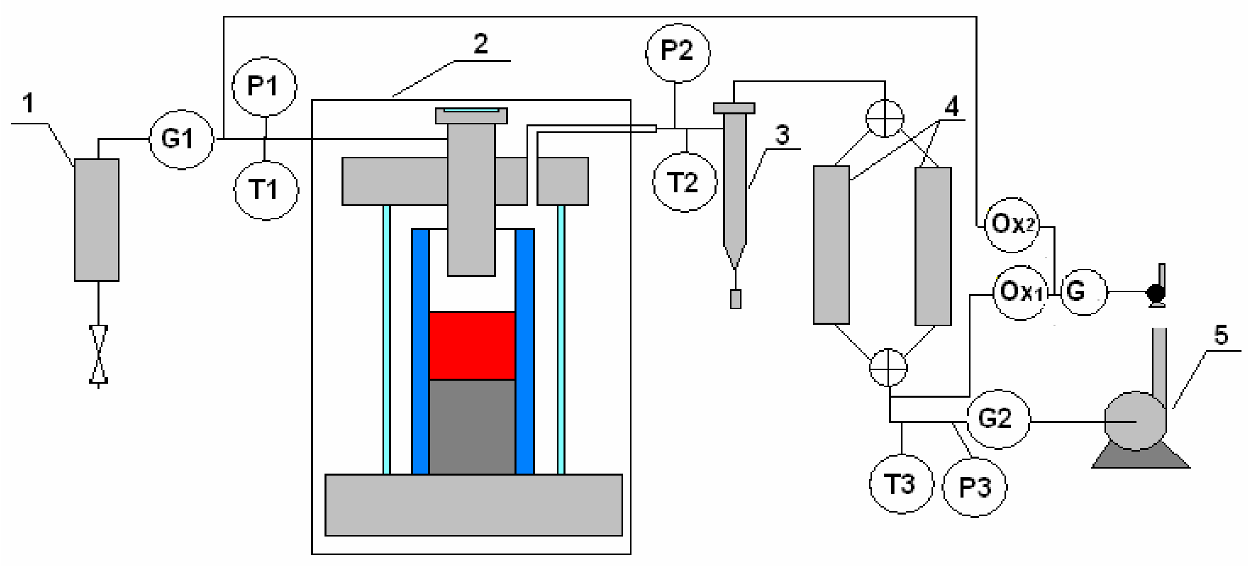

1 – silica gel dehumidifier; 2 – furnace; 3 – cyclone; 4 – Large Area Filter (LAF); 5 – vacuum pump; P1-P3 – pressure transducers; G1,2 – flow rate transducers; T1-T3 – thermocouples; Ox – electrochemical oxygen sensor

Fig. 1.4 – Air in and out diagram

1.2 Materials

The materials used in the test included 20MNMONI 5-5 European vessel steel (Fig.1.5), urania, zirconia and metallic zirconium. Tab. 1.2 offers a comparison of Russian and European vessel steel compositions.

Table 1.2 – Composition of the Russian (15Kh2NMFA-A) and European (20MnMoNi5-5) vessel steels

Steel	Chemical elements content, mass %											
	Al	C	Si	Mn	Cr	Ni	Mo	V	P	S	Cu	Sn	As
15Kh2NMFA-A	-	0.13-0.18	0.17-0.37	0.30-0.60	1.8-2.3	1.0-1.5	0.5-0.7	0.10-0.12	<0.02	<0.02	<0.3	0.0016	<0.003
20MnMoNi5-5	0.010-0.040	0.15-0.25	0.10-0.35	1.15-1.55	0.20	0.45-0.85	0.40-0.55	0.020	0.012	0.012	0.12	0.011	0.025

All metal oxides and metals (charge components) have been checked for the main substance content. In addition, thermogravimetry has shown the oxygen/uranium ratio to be 2.35 for the powdered urania and 2.0 for the ground UO_2 bushings. The composition of corium charge is given in Tab. 1.3.

Fig. 1.5 – Vessel steel blank

Table 1.3 – Corium charge composition

Component	Main substance content, %	Impurities, mass %	Notes
Powdered $UO_{2.35}$ <100 µm dispersivity	>99.9	Fe < 0.03; As < 0.0003; Cu < 0.01; phosphates < 0.002; chlorides < 0.003	Certificate data; thermogravimetry
UO_2 granules sized <5-8 mm	>99.0	Fe<0.03; As<0.0003; CuO<0.01; phosphates <0.002; chlorides <0.003.	Certificate data; thermogravimetry
ZrO_2	$(ZrO_2 + HfO_2)$ > 99.4	$Al_2O_3 < 0.03$; $Fe_2O_3 < 0.05$; $CaO < 0.03$; $MgO < 0.02$; $SiO_2 < 0.2$; $TiO_2 < 0.1$; $P_2O_5 < 0.15$; $(Na_2O+K_2O) < 0.02$	Certificate data
Zr, Hb-1 alloy	Zr>99.0	Nb < 1.0	XRF
Powdered iron	99.9	-	Certificate data

The composition and masses of charge components loaded into the crucible before melting are given in Tab. 1.4.

Table 1.4 – Charge components composition and mass

Purpose	Component	Fraction, µm	Mass, g
Crust imitator	Corium from Pr-MCP4	< 50	150
Main charge	Corium from Pr-MCP4	<1000	1050
	Urania, UO_2	< 100	108.6
	Zirconia, ZrO2		13.0
	Metallic zirconium as the start-up material, Zr	Pieces	28.4
Additional charge	Carbonyl iron	Compressed pellets	265.6
Total:			**1615.6**

The procedure of crucible loading with the charge was as follows: a layer of crust imitator, i.e., 150 g of corium fused in air in a specially performed Pr-MCP4 pretest, composed of 71.0% UO_{2+x}; 29.0% ZrO_2 (mass % here and further in text), with particles dispersivity below 50 µm, were placed on the steel specimen top, and above it followed the remaining corium (1050.0 g, also fused in Pr-MCP4) ground down into 300-500 μm particles mixed with the ground UO_2 bushings (m=108.6 g) and ZrO_2 (m=13.0 g). Metallic Zr (m=28.4 g) was used as the start-up material.

1.3 Experimental procedure

The start-up heating and molten pool formation in air were done at Z_c=20 mm, Z_e=10 mm, where Z_e, Z_c – are distances from the inductor bottom end to the electromagnetic screen and to the welded sections upper edge, respectively (Fig.1.1).

At 620 s, the molten pool depth and bottom crust thickness were measured and found to be 50 and 0.5 mm, respectively. The molten pool surface temperature was 2550-2600°C (Fig. 1.6).

During the period from 650 through 3150 s, the specimen top temperature was smoothly raised (thermocouple readings helped to control this process). To this end, the screen and crucible were shifted for 8 mm (Fig. 1.1, Z_c=12 mm, Ze=10 mm).

At 3150 s, the specimen top temperature was approximately 1000°C (Fig. 1.6). At the same time, the first melt sample was taken and, according to the test plan, from that moment investigation of the vessel steel corrosion kinetics at the interaction with corium through the crust in air was initiated during the 1st regime of the specimen stabilized temperature. At 6380 s, the HF heating automatically switched off, but it was immediately restored. This circumstance has caused a malfunction in the US sensor operation which was rectified by 8860 s, and the vessel steel corrosion investigations were continued.

In order to optimize the power input into the molten pool, the power control feedback system was switched on from 9860 through 11273 s (Fig. 1.7).

At 11273 s, transition to the 2nd specimen temperature regime was made. The specimen top temperature was about 1100°C. In order to compensate for the losses through evaporation, 100 and 50 g of urania were introduced into the melt at 10952 and 13798 s, respectively.

At 14430 s, transition to the 3rd specimen temperature regime was made. The specimen top temperature was about 1200°C (Fig. 1.6). In the end of the regime, melt sample 2 was taken, and then the crucible was shifted for 10 mm (Fig. 1, Z_c=22 mm, Ze=20 mm). It was done to reduce the specimen top temperature and thus preventing corrosion at the next transient stage.

According to the test procedure, the pool composition was changed during the period from 15690 through 20670 s by introducing compressed pellets of metallic iron into the melt. Metallic iron oxidation was controlled by checking readings of the oxygen electrochemical sensor (Ox_1, Fig. 1.9). To limit heating up of the melt due to the exothermic iron oxidation after the introduction of metallic iron into the melt, the inductor voltage was decreased (Fig. 1.7), thus decreasing the power in the molten pool as a consequence (Fig. 1.8). After the dissolution of all iron in the molten pool, the surface temperature was about 2000°C (Fig. 1.6).

At 21580 s, the third melt sample was taken.

At 24000 s, transition to the 4th specimen temperature regime was made. The specimen top temperature was about 1000°C (Fig. 1.6).

At 26490 s, the melt composition was corrected by introducing 50 g of UO_2 and 168 g of ZrO_2 into the molten pool.

At 26617 s, the fourth melt sample was taken.

At 27190 s, transition to the 5th specimen temperature regime was made. The specimen top temperature was about 1100°C (Fig. 1.6).

At 30110 s, transition to the 6th specimen temperature regime was made. The specimen top temperature was about 1200°C (Fig. 1.6).

At 30900 s, the fifth melt sample was taken, and at 31690 s the HF heating was disconnected and the melt was crystallized in air.

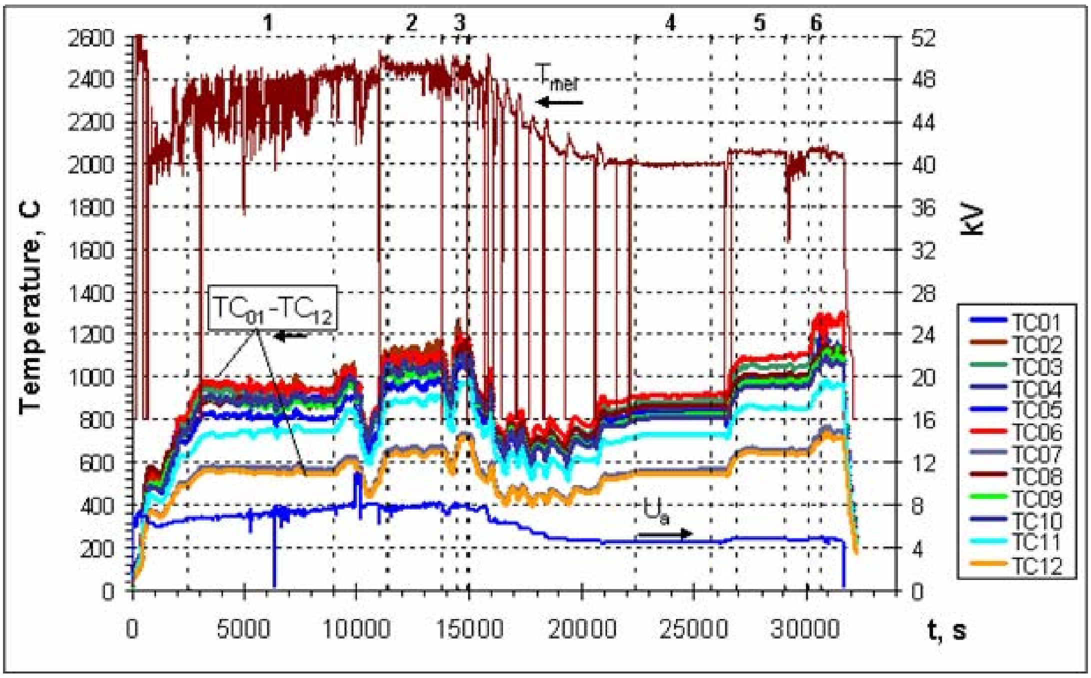

Fig. 1.6 – Pyrometer and thermocouple readings, and the anode voltage time history

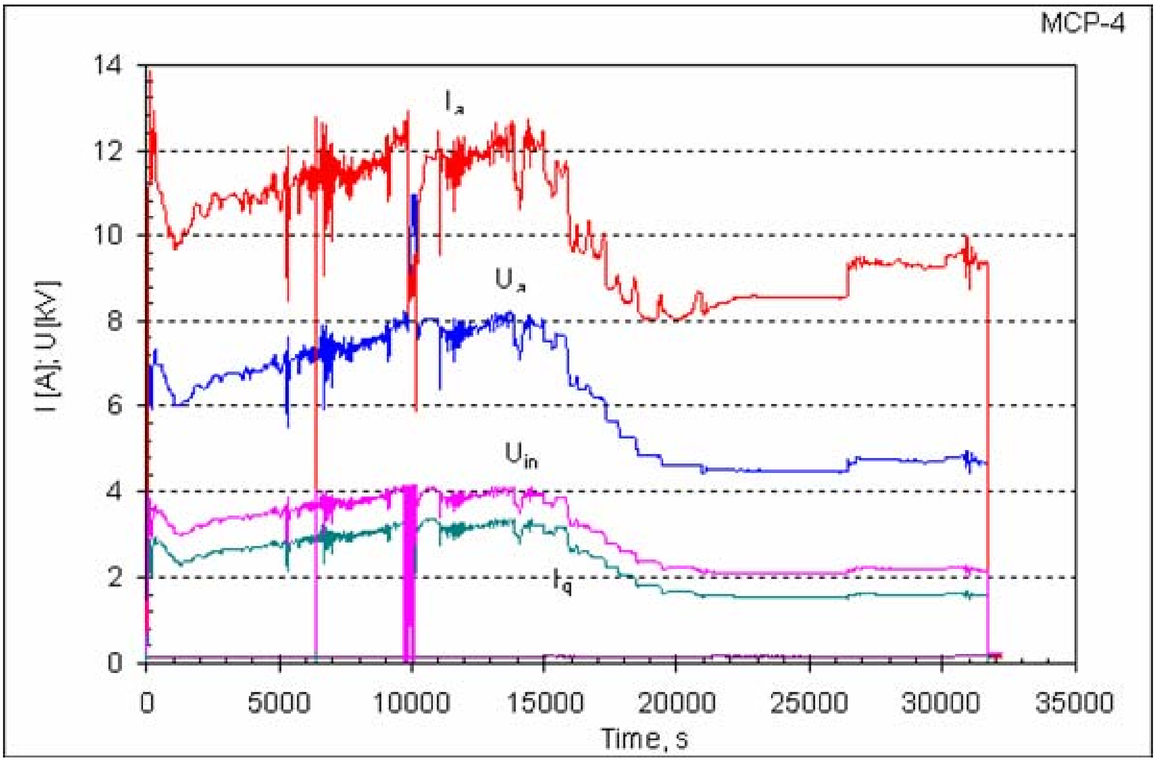

Fig. 1.7 – The time history of anode current and voltage, inductor voltage and grid current of the generator valve

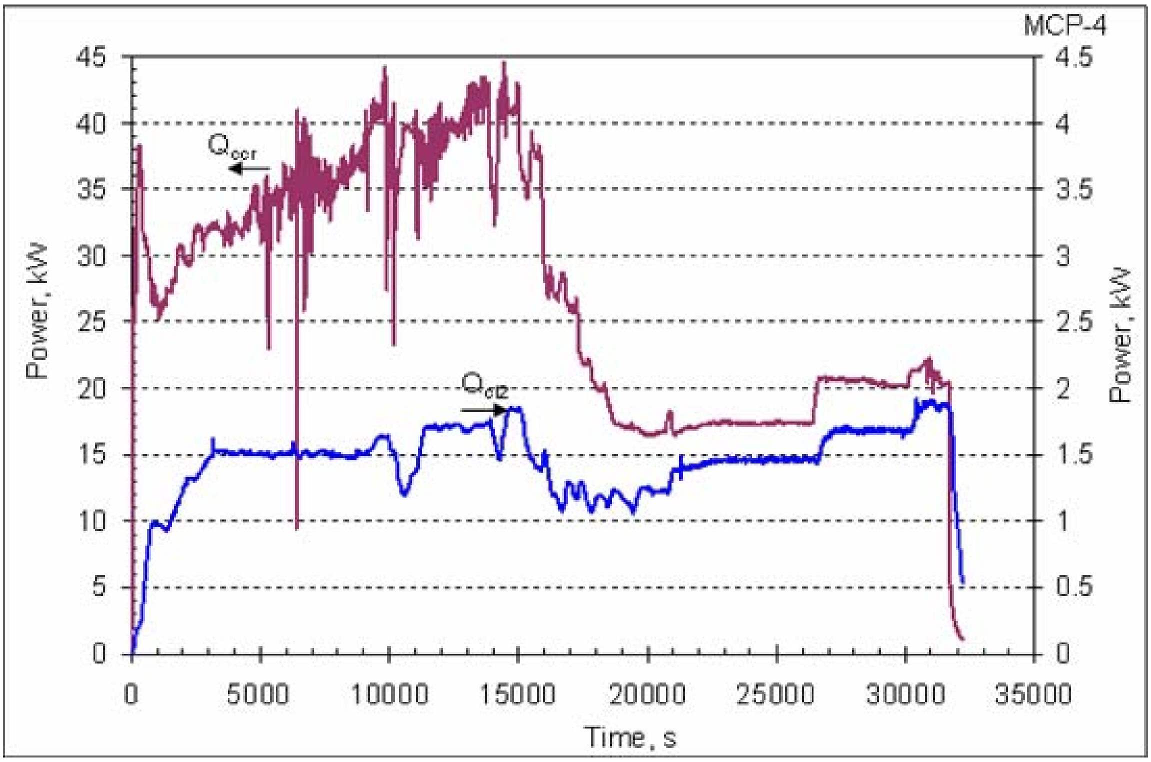

Fig. 1.8 – The time history of the total (thermal and electromagnetic) flux to the crucible and of thermal flux to the calorimeter

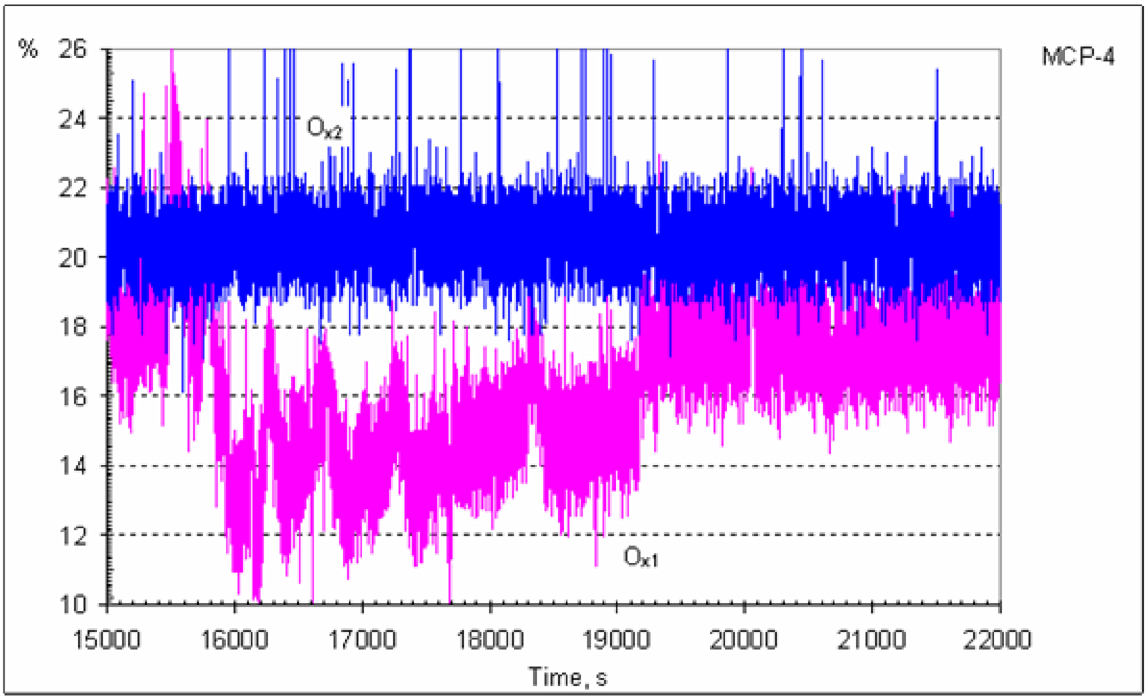

Fig. 1.9 – Oxygen sensor readings

1.4 Ultrasonic measurements of the specimen corrosion

The technique of corrosion depth measuring, i.e., of determining the interaction front position change in time, was the same technique of ultrasonic sounding as that used in previous METCOR tests. The specimen was probed with a pulse-periodic signal with a varying reference frequency. Between pulses, the ultrasonic transducer automatically switched into the reflected signal receiving mode. The distance between the reflecting surfaces (from the specimen top and from the acoustic defect) is

$$D = 0.5 s \Delta t\ , \qquad (1.1)$$

where s is the velocity of sound in the specimen;

Δt is the time period between the radiated and reflected signals.

The dependence of sound velocity on temperature was determined during the regimes of specimen heating and cooling, in the absence of its corrosion.

Fig. 1.10 shows reflected signals as seen on the monitor, that is, two groups of sinusoidal signals. The left group represents the signals from the defect, while the right one – those from the specimen top. The reference frequency is the ultrasonic transducer resonance frequency. The frequency content of groups differed due to differences in the reflecting surfaces shape.

To determine the time interval, in-phase half-waves were chosen (one per group) and two characteristic points were marked on each chosen half-wave, i.e., one at the intersection with the zero line, and the other at the amplitude maximum. Later on, time lag was monitored for a pair of corresponding points (any pair), and the distance from the defect to the specimen top (reducing in time due to steel corrosion) was calculated taking the velocity of sound at the current temperature in the specimen into account. The calculations were made by processing the incoming information on the computer. Sensitivity of determining spatial position of the interaction front was 0.01 mm.

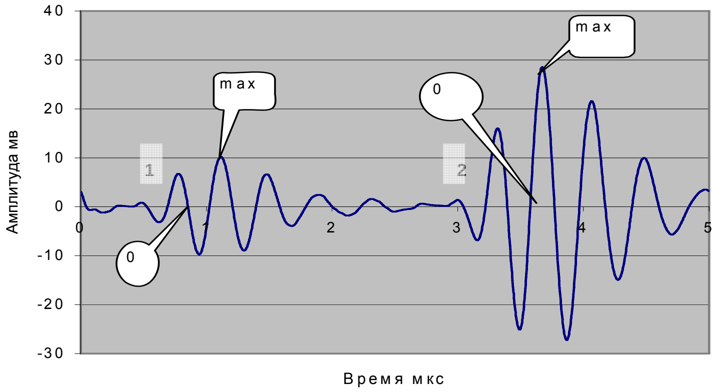

1 – signal reflected from the defect; 2 – signal reflected from the specimen top; «max» – maximum positions of the in-phase half-waves; «0» – position of zero points of in-phase half-waves

Fig. 1.10 – Specimen echogram during the interaction with molten corium

Fig. 1.11 shows the results of on-line measurements. The sufficient precision of US measurements is confirmed by the fact that the corrosion depth registered by the end of the test is close to the value obtained from the profilogram in Fig. 2.10. This value (in the US sensor sighting spot, ∅ 15 mm) was approximately 5.7 mm.

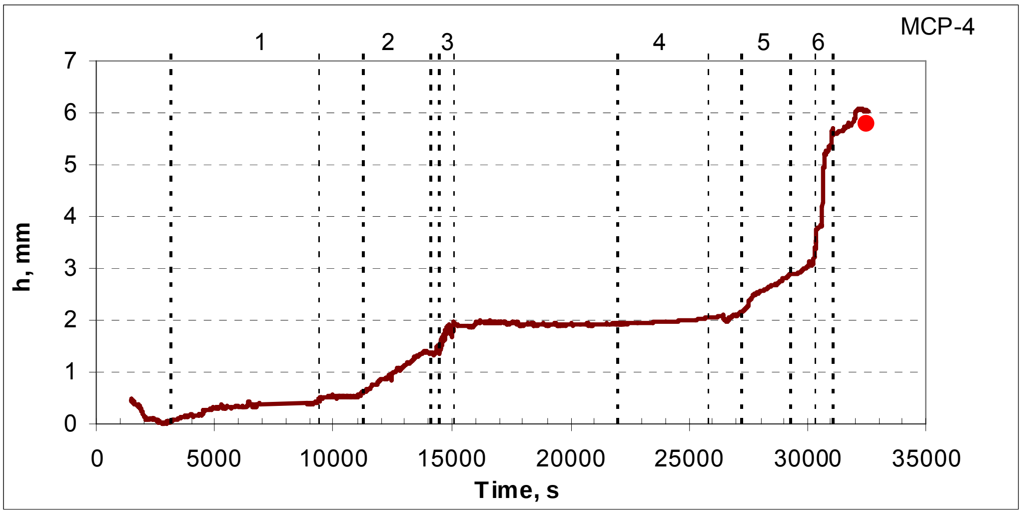

● – posttest measurement; —— – on-line measurement

Fig. 1.11 – Depth of specimen corrosion

2 POSTTEST ANALYSIS

2.1 Specimen temperature condition

In order to determine steel corrosion conditions and to analyze experimental results, calculations of the specimen temperature conditions were performed in the same way as in the previously conducted tests. The calculations employed a finite-element program that implemented solution of a stationary heat conduction equation in the axis-symmetrical formulation. The specified boundary conditions were 1) the temperature on the inner surface of the top calorimeter (see Fig. 1.1.) estimated at 100°C (the insignificant error of its determination has practically no influence on the calculation results), 2) the temperature on the inner surface of the bottom calorimeter (20°C), and 3) the temperature on the outside surface of peripheral thermal insulation layer accepted as equal to the average temperature of cooling water. Thermal conduction of 20MNMONI 5-5 steel, from which the specimen was produced, is given in Tab. 2.1.

Table 2.1 – Thermal conduction of 20MNMONI steel

T,°C	20	100	200	300	400	500	600
λ, W/(m K)	44.3	44.0	42.9	40.8	38.4	36.8	33.9

The heat flux to the specimen top and thermal conductivity of the lateral insulation were varied in the calculations to provide the best agreement between the calculated and measured temperatures in the specimen at the locations of thermocouple junctions. The distribution of the incoming heat flux along the radius of the specimen upper top was specified according to the melt thermal hydrodynamics calculated jointly with solving the electromagnetic problem in tests MC10 and MC11 [3]. Like MCP-4, these tests investigated the interaction of UO_{2+x}-ZrO_2 and UO_{2+x}-ZrO_2-FeO_y coriums with steel specimens under conditions close to those in MCP-4.

The temperature and heat flux at the specimen top in the US sensor sighting spot have been calculated for each regime of the test. During a regime, corrosion was changing the specimen surface position and shape, so these data for calculations were taken for the middle of each regime time interval and determined by the US measurements. Thermocouple measurements for each regime have been time averaged. For the 6th regime (approximately from 30200 through 31000 s), during which the specimen temperature condition and corrosion depth were significantly changing, calculations were made for different time instants and the obtained results averaged. Precision of the specimen temperature condition numerical modeling and, therefore, of determining the required temperature and heat flux at the specimen to may be judged by comparing the calculated values with thermocouple readings given in Fig. 2.1. Also, Fig. 2.1 offers the calculated values of Q_c and experimentally determined values of thermal power (Q_e) from the specimen into the top calorimeter, the discrepancy of which does not exceed 15%.

Regime 1

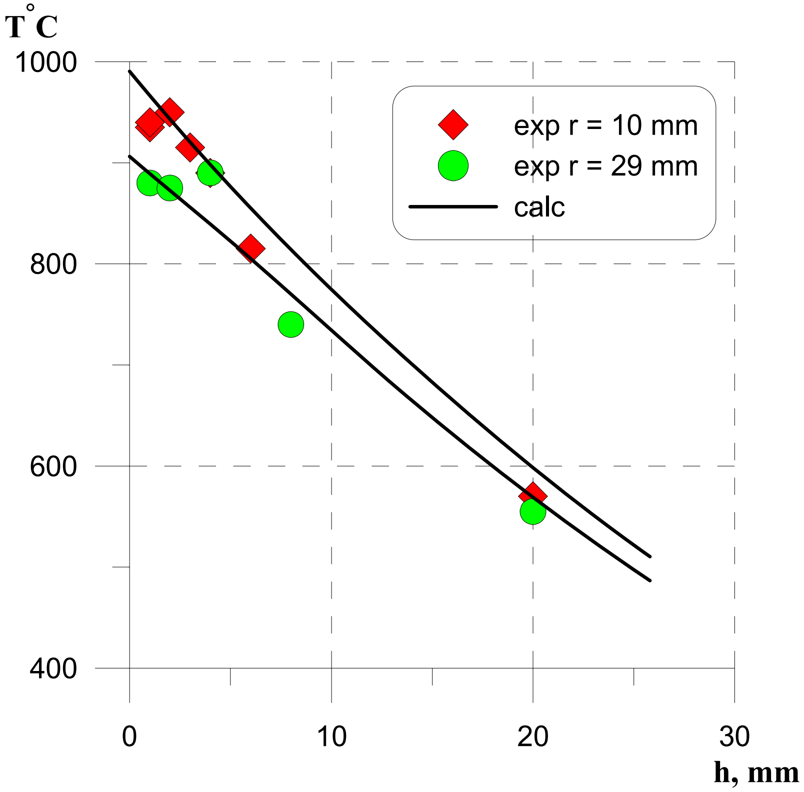

Q_c=1.25 kW, Q_e=1.5 kW

Regime 2

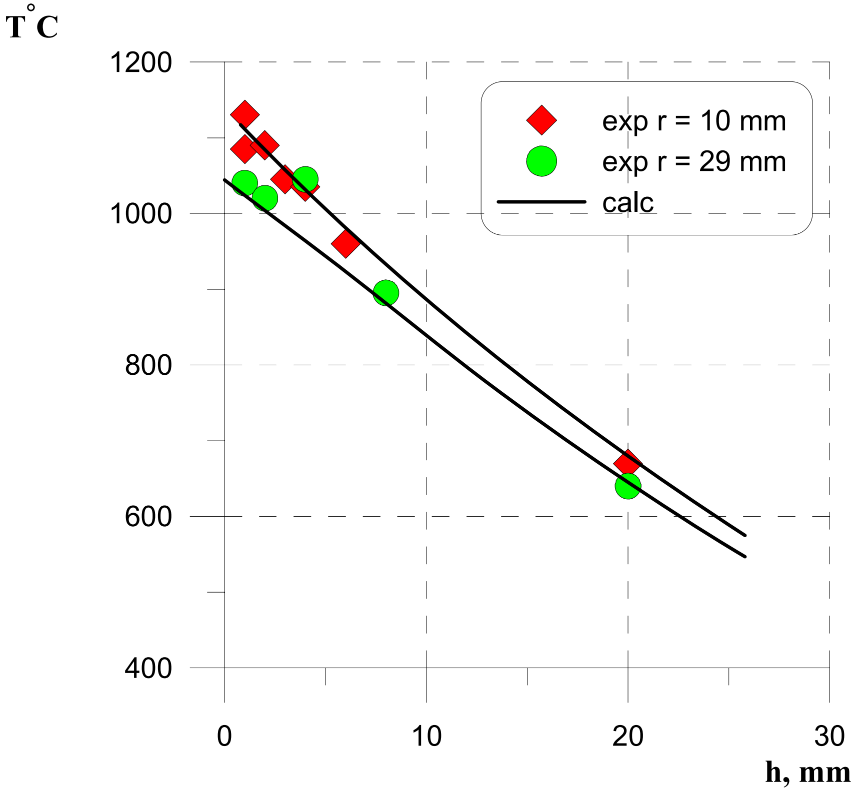

Q_c=1.47 kW, Q_e=1.6 kW

Fig. 2.1 – Temperature distribution along the specimen height

Regime 3

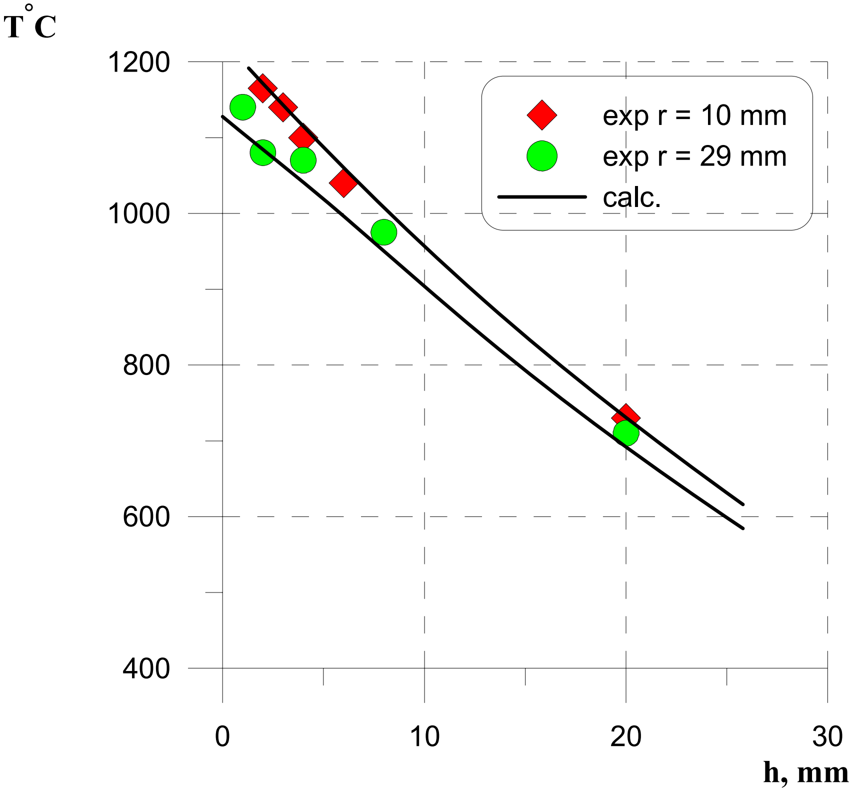

Q_c=1.59 kW, Q_e=1.8 kW

Regime 4

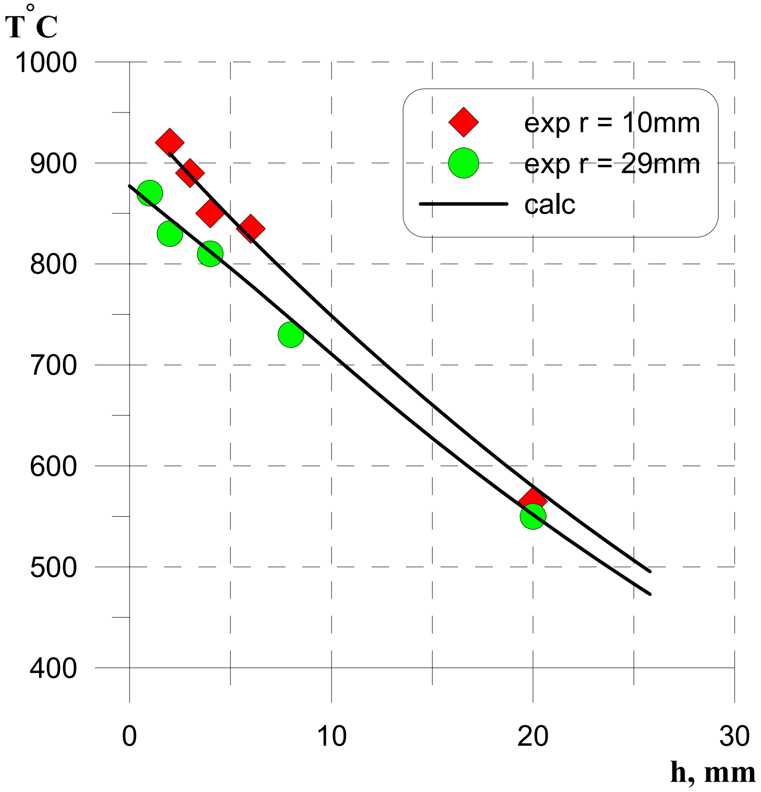

Q_c=1.25 kW, Q_e=1.5 kW

Fig.2.1, continued

Regime 5

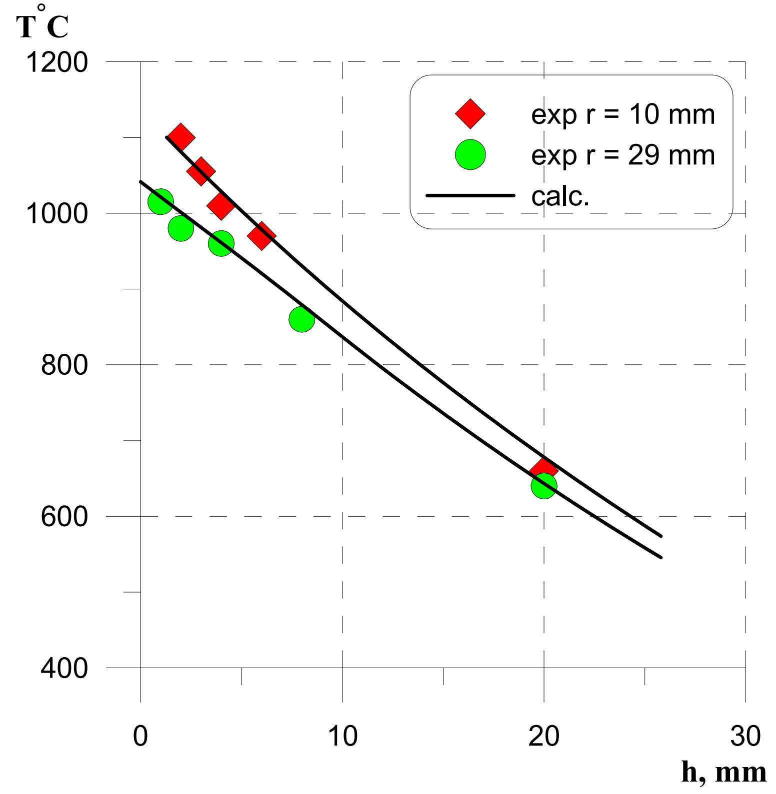

Q_c=1.48 kW, Q_e=1.7 kW

Regime 6

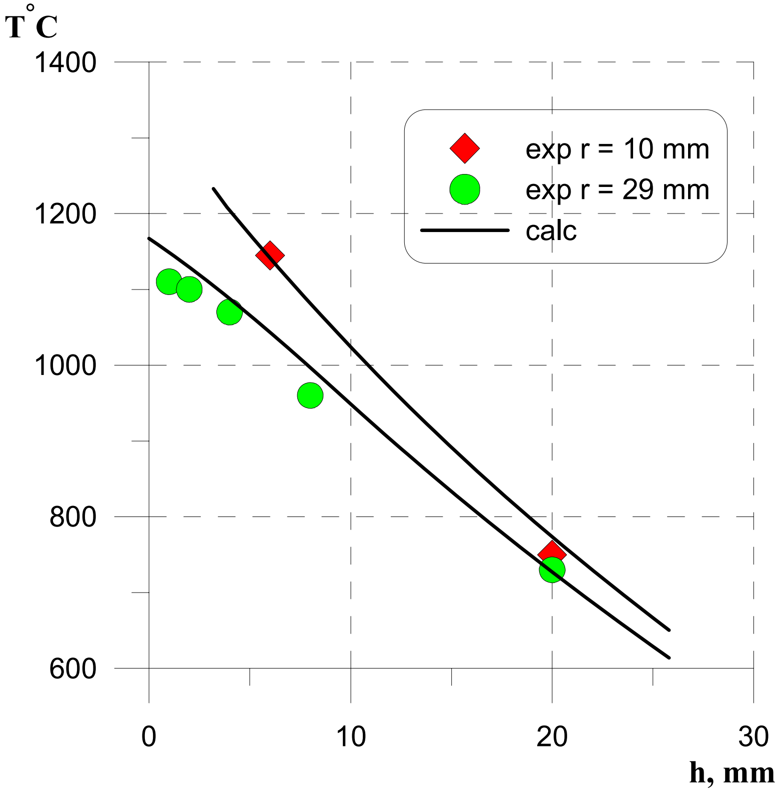

Q_c=1.67 кВт, Q_e=1.8 кВт

Fig.2.1, continued

Tab. 2.2 offers the calculated temperatures and heat fluxes, as well as the corresponding corrosion rates for all regimes (averaged, in the USS sighting spot). The error of said parameters determination was 20% for q and W, while for T it was 30°C.

Table 2.2 –MCP-4 results

Regime No.	Steel surface temperature, T, °C	Heat flux, q, MW/m^2	Corrosion rate, $W\times10^6$, m/s
1	1005	0.77	0.056
2	1130	0.86	0.3
3	1200	0.91	0.81
4	920	0.71	0.028
5	1080	0.82	0.32
6	1150	1.0	3.0

2.2 Physicochemical analysis

2.2.1 Ingot macrostructure

When disassembling the furnace after MCP-4, the crucible sections were found to be coated with a layer of aerosols and a crust was located above the ingot (Fig. 2.2, 2.3). The corium ingot extraction from the furnace resulted in its destruction and separation from the specimen (Fig. 2.4). Ingot fragments are shown in Fig. 2.5. Their shape made it possible to restore their mutual position and that relative to the steel specimen. The main part of the oxidic ingot was later restored (Fig. 2.6). The steel specimen top after the test is shown in Fig. 2.7.

A fragment of the oxidic ingot and steel specimen were separately embedded in epoxy and used for preparation of templates to be subjected to analyses.

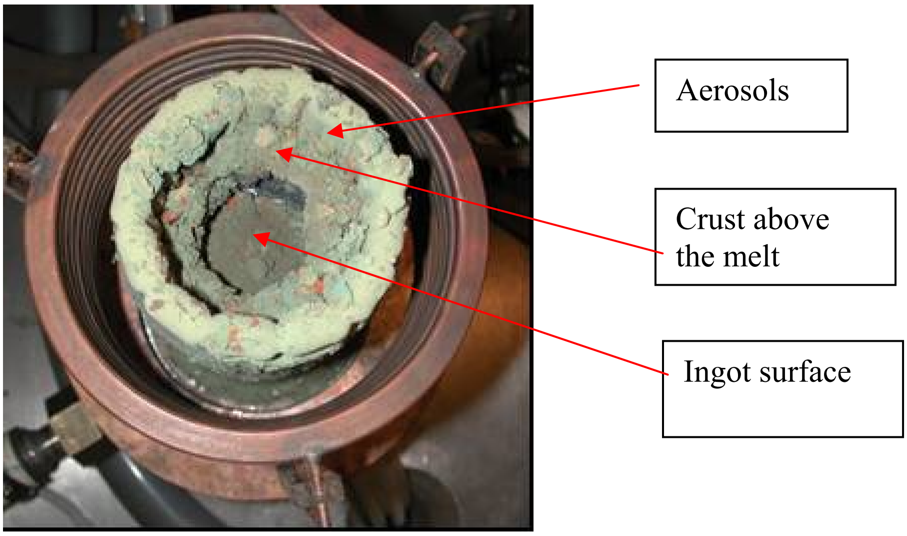

Fig. 2.2 – Top view of the crucible during furnace disassembling

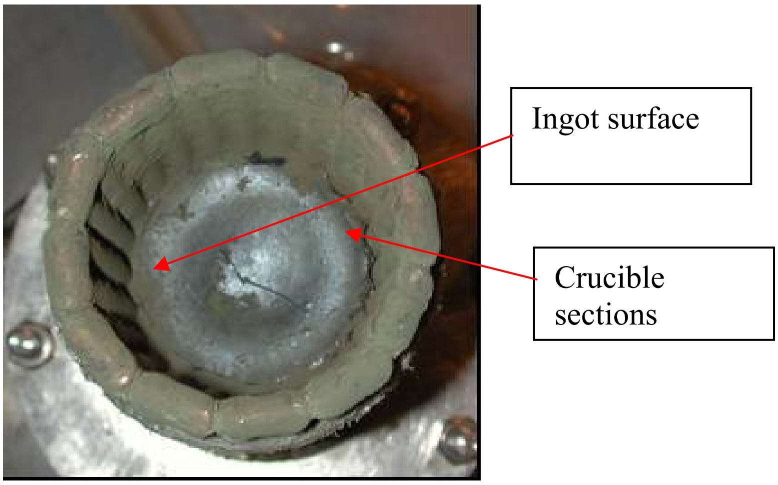

Fig. 2.3 – Ingot surface

Fig. 2.4 – Oxidic ingot fragment adjacent to the specimen

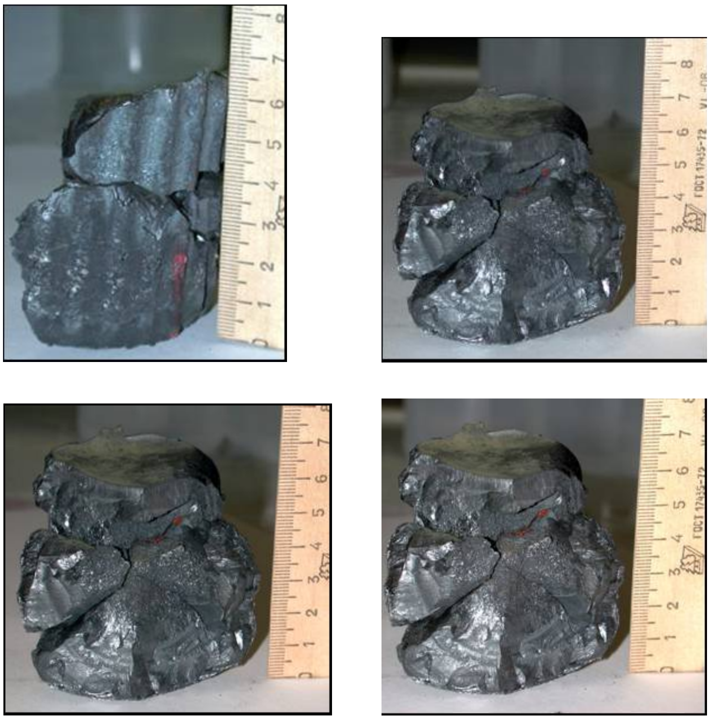

Fig. 2.5 – Ingot fragments

Fig. 2.6 – Reconstructed oxidic ingot

Fig. 2.7 – Steel specimen top after the test

2.2.2 Material balance of the test

In order to make the material balance, the initial charge components and fused products were carefully collected, weighed with an accuracy up to 0.1 g and then analyzed for the main components content. Material balance for MCP-4 is given in Tab. 2.3.

Table 2.3 – MCP-4 material balance

Introduced into the melt, g		Collected after the test, g	
UO_2	308.6	**Ingot**	1493.4
ZrO_2	29.8	**Crust above the melt**	185.0
Zr	28.4	**Aerosols**	277.7
Crust[2)]	150.0	**Dry spillages**[1)]	139.0
Ingot from Pr-MC4[3)]	1050.0	**Sample 1**	2.4
Powdered iron	265.6	**Sample 2**	5.3
Fianite	56.2	**Sample 3**	7.4
ZrO_2(fine-dispersed)	28.9	**Sample 4**	2.9
		Sample 5	6.9
		Rod sample	4.3
Σ	**1917.5**	**Σ**	**2124.3**
Debalance	**+206.8**		

[1)] – Dry spillages include charge material (lateral crust), ZrO_2 (fine-dispersed) and fianite;

[2)] – The corium fused in air in Pr-MCP4 pretest was used as the crust. The crust composition determined by chemical analysis is presented in Tab. 2.5;

[3)] – The composition of ingot from Pr-MCP4 (chemical analysis data) is presented in Tab. 2.5.

Tab. 2.3 clearly shows that the debalance value was +206.8 g, which is explained, in the first place, by oxidation of the iron introduced into the melt and by urania oxidation ($U^{+4} \rightarrow U^{+6}$ transition), since the test was performed in air, as well as by transition of some iron from the steel specimen into molten corium.

Tab. 2.4 contains masses of aerosols collected from different components of the furnace and gas evacuation system.

Table 2.4 – Masses of aerosols collected during the test

Item	Sample weight mass, g
LAF 1	65.1
LAF 2	21.7
LAF 3	18.0
Aerosols from quartz tube (Fig. 1.1, Point 6)	39.9
Aerosols from the pyrometer shaft (Fig. 1.1, Point 4)	0.4
Aerosols from crucible sections (Fig. 1.1, point 5)	73.4
Aerosols from cyclone (Fig. 1.4, Point 3)	30.5
Aerosols from tubes	28.8
Total	277.7

Tab. 2.5 offers the results of chemical analysis of an average samples from the ingot from Pr-MCP4. The corium fused in Pr-MCP4 (150.0 g, >50 µm dispersivity) was used as the crust imitator. In order to reduce the volume of loaded materials, the corium that left from Pr-MCP4 was crushed down into 300 – 500 µm-sized particles and used in MCP-4 as the charge material.

Table 2.5 – Chemical analysis of an ingot average sample from Pr-MCP4

Element	Content, mass %
U^{+4}	50.10
U^{+6}	12.33
Zr^{+4}	20.99
Impurities and O[1)]	16.58

[1)] – impurities and oxygen determined from the residue.

2.2.3 Fused products chemical analysis

Upon completion of the test, the oxidic ingot, melt samples taken during the test, crusts, the rod sample and dry spillages were individually crushed down into particles below 200 µm, and then average samples were taken by quartering. The average samples were further crushed to particles not exceeding 50 µm and examined for the content of U, Fe and Zr ions. The previously elaborated technique [3] has been used, the essence of which is in taking a 0.1 g sample weight of ground corium, dissolving it in a mixture of concentrated orthophosphoric and sulphuric acids (1:2) in flowing argon, and then determining the content of Fe^{2+} and Fe^{3+} by photocolorimetry with orthophenanthroline, and that of U^{4+} and U^{6+} – using arsenazo III [4÷6].

To determine Zr^{4+}, a 0.1÷0.5 g aliquot was fused with (3.0±0.5) g of potassium pyrosulphate at (900±25)ºC until the appearance of a transparent alloy, which was further dissolved at heating it in 200÷250 ml 1M solution of sulphuric acid. Then zirconium was determined as Zr^{4+} by photometry with orange xylenol. The method of total Zr determination is based on the formation of a colored complex compound of Zr (IV) and orange xylenol in the solution of sulphuric acid and molar concentration of equivalent 0.3 – 0.4 mole/dm^3 [7÷9]. The evaluation of zirconium is not complicated by large quantities of Mo, W, U, Zn and Ti, as well as impurities of Fe (up to 50 μg), Pb, Ni, Cu, Th and Ta (>100 μg) [8, 9].

The technique of U+4 and U+6 determination is meant for the determination of uranium microquantities [5, 6] with a sensitivity of 0.04 μg/ml. The technique is based on the formation of stained compounds of the tetravalent uranium and arsenazo III in the 4 N HCl medium. Uranium is reduced by granulated zinc in the presence of ascorbic acid. At the interaction with arsenazo III, the tetravalent uranium yields a complex of green colour, while with the excessive reagent the observed colour is violet of different shades. Spectrophotometry is best with a 2 to 5-time higher molar content of the reagent. Staining occurs almost instantly and is stable for at least two hours. The technique allows determination of the tetravalent uranium and the total uranium in a solution. The quantity of the hexavalent uranium is calculated from the difference between the content of the total and tetravalent uranium.

The method of Fe^{2+} and Fe^{3+} determination is meant for the determination of iron oxides content in samples of the uranium-bearing corium without uranium separation [4]. The range of identified iron concentrations is 0.5-2.0 mg/dm^3. The total relative error of the method does not exceed ±3%, provided the measured optical densities are within 0.2-0.6 range. The method is based on the reaction of orthophenanthroline (1.10-phenanthroline) with ferrous iron ions, which yields a complex compound with an orange-red colouring. The colour intensity is proportionate to the concentration of iron. Since the bond strength of the complex compound is high (formation constant is $9.8 \cdot 10^{21}$), optical density does not depend on pH in the 2÷9 range. Colouring develops rapidly at pH=3.0÷3.5 in presence of excessive orthophenanthroline and keeps stable within several weeks. In more acid solutions, the colouring develops slower and is less intense. The direct iron determination is possible at its mass concentration from 0.5 to 2.0 mg/dm^3 [10, 11]. The method allows separate determination of ferrous iron and total iron in a solution. The amount of ferric iron is calculated from the difference between the content of total iron and iron (II) [10, 11].

The error of U content determination by photocolorimetry did not exceed 5 relative %, and that of Zr and Fe determination was not above 3 relative %.

Tab. 2.7 offers the results of fused products chemical analysis.

Table 2.6 – Chemical analysis of fused products from MCP-4

Sample	**Content, mass %**						
	Fe^{2+}	**Fe^{3+}**	**∑ Fe**	**U^{4+}**	**U^{6+}**	**∑ U**	**∑ Zr**
Sample 1	not determined	not determined	not determined	48.82	11.65	60.47	23.0
Sample 2	not determined	not determined	not determined	49.85	6.63	56.48	26.11
Sample 3	16.30	5.04	21.34	39.72	1.28	41.0	18.70
Sample 4	12.10	5.94	18.04	40.72	2.03	42.75	18.55
Sample 5	14.84	4.54	19.38	37.86	5.05	42.21	17.57
Ingot top	15.8	1.90	17.70	40.85	2.13	42.98	17.22
Ingot bottom	15.64	2.36	18.0	42.15	1.52	43.67	17.79
Ingot pieces	15.40	1.64	17.04	37.44	5.61	43.05	18.56
Probe	not detected	not detected	-	49.58	7.27	56.85	20.24
Crusts	4.72	0.28	5.06	40.91	21.73	62.64	11.24
Dry spillages	2.0	not detected	2.0	25.32	6.95	32.27	43.35

2.2.4 Specimen metallography

Dimensions of the initial specimen were measured with calipers with a scaling factor of 0.02 mm (20 µm) and the MBS-9 stereoscopic microscope with a 14 µm scaling factor and x50 magnification. The dimensions necessary for determining the steel specimen corrosion depth after the test are presented in Tab. 2.7 and shown in Fig. 2.8, where A is the distance to the first groove in the specimen lateral surface, B is the distance to the reference hole (acoustic defect) axis, and D is the reference hole diameter. The places of measurement are shown in Fig. 2.8.

Table 2.7 – Steel specimen measurements (mm)

A_1	A_2	A_3	A_4	B_1	B_2	D_1	D_2
3.05	3.05	3.05	3.05	8.95	9.00	2.10	2.1

Specimen length L = 104.0 mm

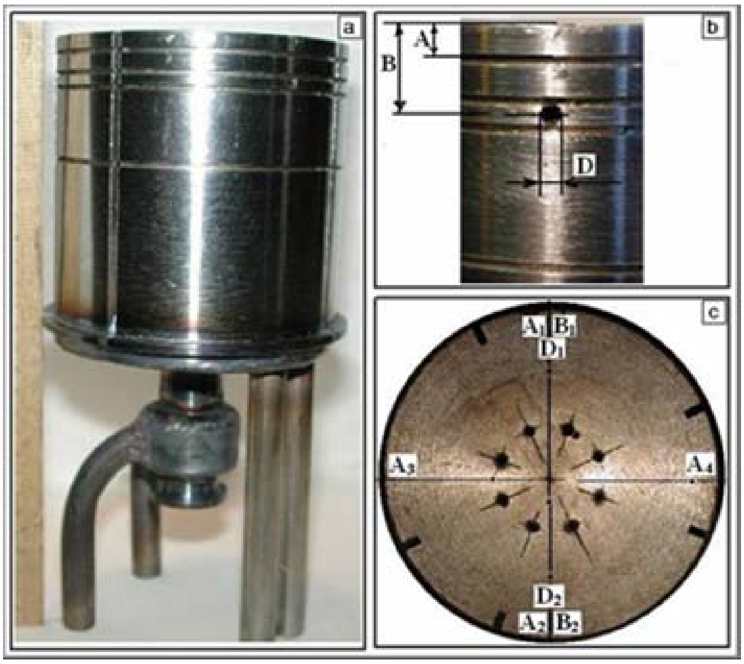

Fig. 2.8 – The steel specimen (a), fragments of steel specimen lateral surface (b) and upper top (c) before MCP-4

For a comparative analysis of steel microstructure before and after the test, initial characteristics were studied on a reference specimen ∅40×4 mm. The steel 16MND5 (20MNMONI55-3 according to the marking on the blank) belongs to pearlitic steels; its microhardness according to Hv_{50} = 180 – 200 kgf/mm^2 (Fig. 2.9).

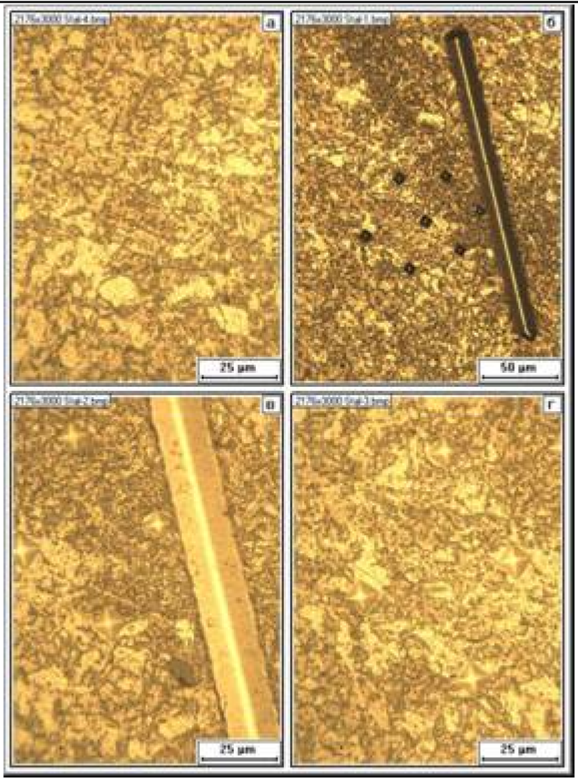

Fig. 2.9 – Fragments of the initial steel microstructure with the diamond pyramid imprints

After the test, a template from the axial cut of the oxidic corium and steel specimen was prepared. The steel specimen template was used for measuring the maximum depth of specimen ablation from the upper top.

Fig. 2.10 presents the steel specimen longitudinal axial section after the test, with the revealed macrostructure and regions marked for microstructural studies.

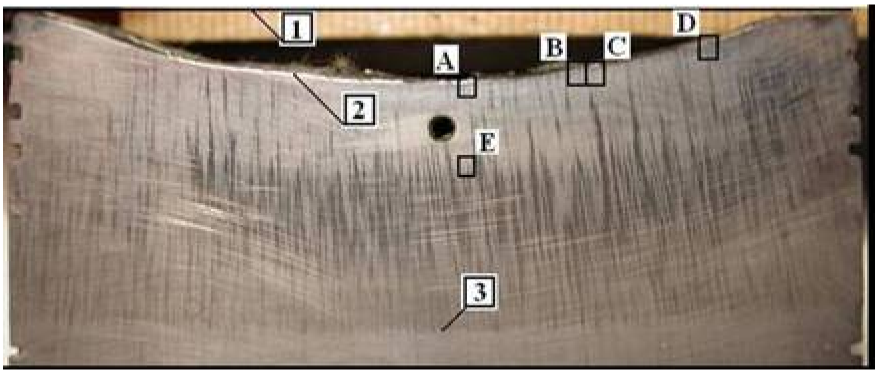

1. reference plane of the steel specimen initial upper top;
2. profile of specimen upper top after the test;
3. boundary of the zone of molten corium thermal influence on steel macrostructure;

A – E regions chosen for microstructural studies.

Fig. 2.10 – Steel specimen axial cut near the upper top

Direct measurements along the specimen longitudinal section were made using the MBS-9 stereoscopic microscope at x50 and x100 magnifications. The scale factor of micrometer screws is 0.01 mm (10 µm). The measurement error is below ±10 µm; it was determined with the stage micrometer. The position of the initial upper top plane was determined from the groove made in the specimen lateral surface at 3.0; 7.0 and 25.0 mm from the upper top.

The macrosection images were processed on the computer and a profilogram of the specimen upper top after the test plotted (line 2, Fig. 2.11). Dimensions marked in the profilogram in Fig.2.11 are as follows: specimen width (diameter) is plotted along the X-line, and the distance from the reference plane of the initial top (line 1) – along the Y-line (top-down). The distribution of corrosion depth along the specimen diameter is close to axis-symmetric. Corrosion irregularity is determined by temperature reduction from the center to the periphery due to heat removal from the specimen lateral surface to the cold crucible sections.

According to the results of measurements, the maximum depth ablation amounted to 5.7 mm, while the zone of molten corium thermal influence on steel macrostructure spread to a depth of up to 23.4 mm along the specimen axis in its central part. Like in tests with the Russian reactor steel, position of boundary 3 may be associated with the temperature boundary of the eutectoid composition in the Fe-Fe_3C system and correspond to the ~730°C isotherm. However, changes in the specimen temperature condition during the test make it impossible to link said temperature to a particular regime out of the 6 used in the test and use as a reference point in a numerical model of the specimen temperature condition.

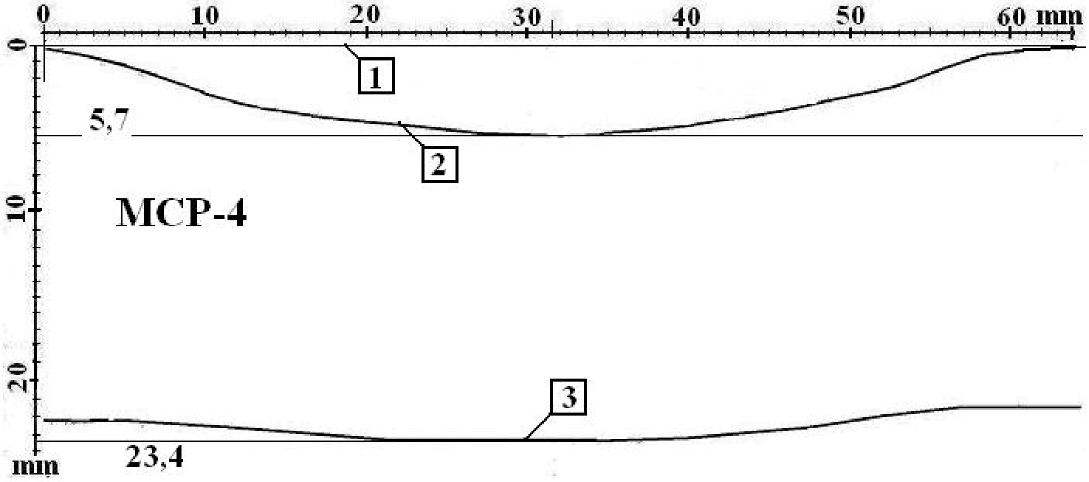

Fig. 2.11 – Profilogram of the steel specimen upper top in the axial section plane (designations correspond to those in Fig. 2.10)

Templates grinding and polishing was done according to the standard technique. To reveal the microstructure, the prepared polished section was treated with etchants, and used metallographic microscopes for quality control. The combined use of etchants for the pearlitic and austenitic steels [12] displayed both macro- and microstructure of the zone of molten corium high-temperature influence of steel and identified microstructure of steel.

When studying the microstructure, surfaces of polished sections were photographed with a NIKON digital camera coupled with the MBS-9 stereoscopic microscope at x50 magnification. The specimen microstructure was photographed using a high-resolution camera (capturing images of polished section surface fragments for storing in the computer) coupled with the METALLUX metallographic microscope at x200, x400 and x900 magnifications. The image scale was determined during photographing for each magnification with the stage micrometer with the scale factor of 10 µm.

The section etching for revealing its microstructure yielded vertical strips of uneven etching (Fig. 2.10), however, no differences in microstructure in dark and light strips were found. Figs. 2.12 – 2.14 show steel microstructure images from different specimen zones, marked by rectangles in Fig. 2.10.

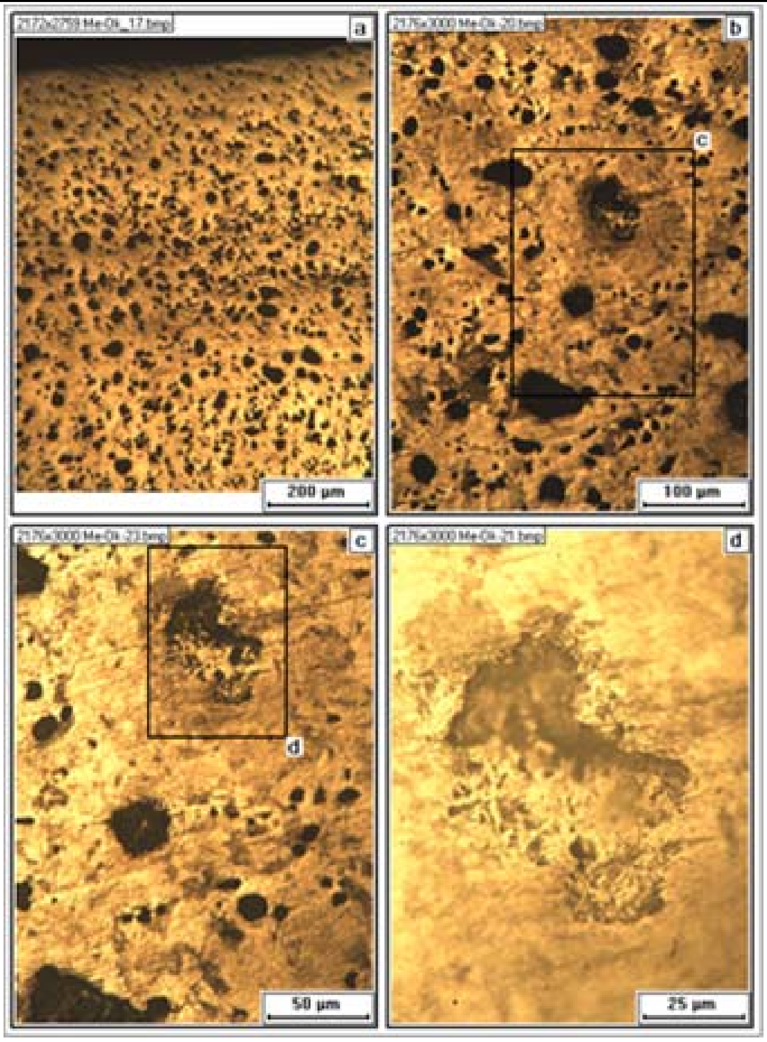

Fig. 2.12 – Steel microstructure near the specimen upper top (area A, Fig. 2.10) with an enlarged fragment (d)

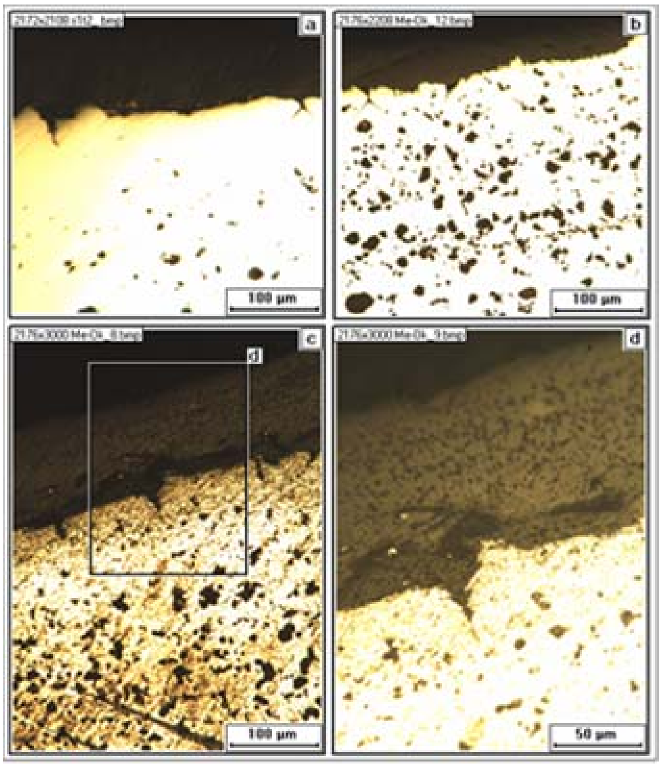

Fig. 2.13 – Steel layers near the surface (areas B, C, D, Fig. 2.10)

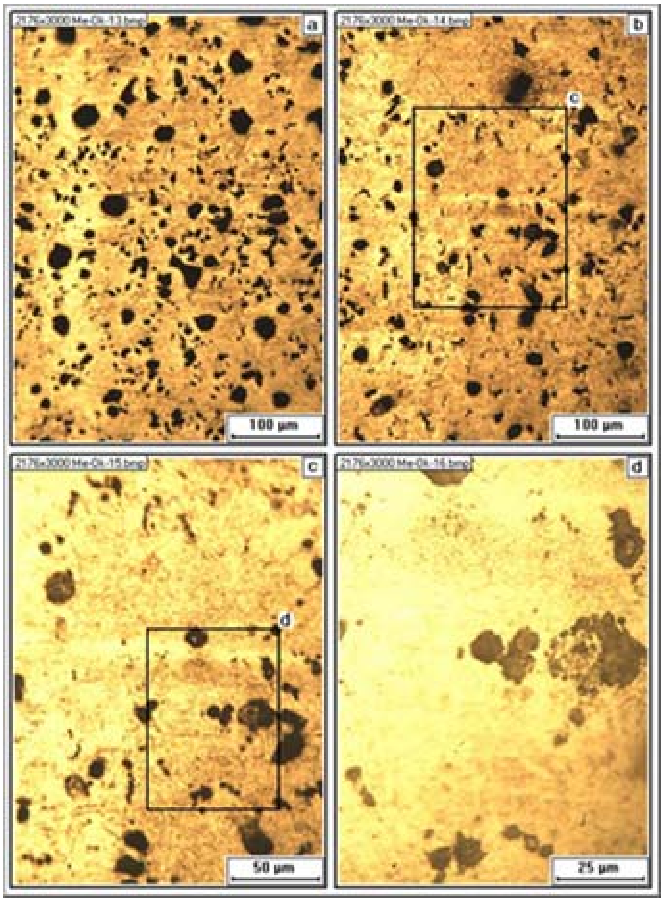

Fig. 2.14 – Steel microstructure (area E, Fig. 2.10) with an enlarged fragment (d)

An analysis of microstructure in the specimen upper top layers close to the surface allows a supposition about structural and phase transformations and carbon redistribution between structural components in the area between curves 2 and 3 where steel heats up above the critical point Ac_3 (723°C). The newly formed microregions with a higher carbon content (the “pearlitic points”) are seen as pores in the polished section at x400. Also, the polished section shows the forming microareas with an increased carbon content (Fig. 2.12, see the area marked by a rectangle) in which a more stable ferritic-pearlitic structure is appearing (Fig. 2.12d). A ferritic structure with the minimal carbon content has formed around the “pearlitic points”.

The specimen macro- and microstructure between curves 2 and 3 has underwent changes as a result of carbon, chromium and other alloying elements redistribution and local formation of a “new” ferritic-pearlitic structure (Fig. 2.12 and Fig. 2.14). Depending on the content of carbon in the formed “pearlitic points” and on the cooling rate, different modifications of pearlite can be obtained, e.g., sorbite, troostite or martensite (even with the content of carbon as small as this one). However, the bulk steel in this area has a low carbon content. Such a change in microstructure may lead to inhomogeneity of mechanical properties, to a lower strength and hardness of steel, along with the decreased impact elasticity and tensile strain.

2.3 SEM/EDX analysis

Fig. 2.15 shows a polished section of the steel specimen with a layer of surface corrosion. The greater part of the corrosion layer has separated from the metallic part together with the oxidic ingot as a result of thermal shrinkage of the latter. It should be noted that the boundary of steel corrosion is smooth and thus evidences the achievement of the stable-state condition by the corrosion front structure. The results of SEM/EDX analysis of the marked regions are presented in Fig. 2.16-2.23 and in Tabs. 2.8-2.10.

According to the EDX data, the European steel composition (Tab. 2.8) in mass % is 96.1±0.6 Fe, 1.7±0.1 Mn, 0.5±0.2 Mo, 0.3±0.2 Si, 1.1±0.2 Ni, 0.3±0.1 Cr. The content of Mn and Ni is by several tenths of one percent higher than that indicated in the European steel certificate (Tab. 1.2). The discrepancy may be due to the fact that the zone for analysis was chosen close to the corrosion boundary where concentration of these components may be higher. Also, it may be an error due to the application of reference-free analysis (of the fundamental parameters method).

Let's consider the interaction zone structure along the steel-crystallized corium line.

The layer immediately adjacent to steel (Fig. 2.17, area 2-1-1, Fig. 2.19, area 5-1, Fig. 2.20, area 6-1, Fig. 2.22, areas 7-1 and 9-1, Fig. 2.23, areas 10-1 and 12-1) along the entire polished section length shows the presence of at least four phases, that is a γ-(Fe,Ni)-based phase (Tab. 2.10, points P1-P4), wustite-based phase (Tab. 2.10, points P5-P7, P15, P16), fayalite-based phase (Tab. 2.10, points P8-P10), and a Fe_3MoO_4–based phase (Tab. 2.10, points P11-P14). The fayalite-based phase is mostly accumulated immediately at the boundary with steel and in the intergrain space (e.g., Fig. 2.20). This layer thickness is assessed at ~10 μm. The main phase coexisting with fayalite is wustite. Above the considered zone, there is a layer with fayalite as the main phase and with phases based on Fe_3MoO_4, γ-(Fe,Ni) and fayalite in the intergrain space (e.g., Fig. 2.19). This layer thickness varies from ~50 μm at the template periphery down to ~10 μm in the zone of area 6 (Fig. 2.15). This zone could not be found in the central part. Only small fayalite-rich zones have remained in the intergrain space of steel (Fig. 2.23, area 12-1).

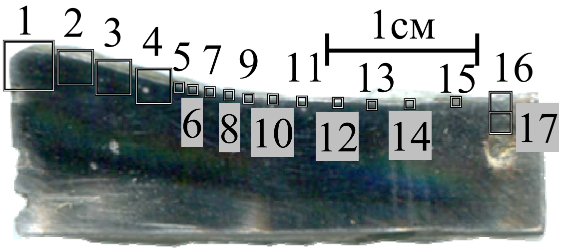

Fig. 2.15 – Polished section of the metallic part from MCP-4 with areas marked for SEM/EDX investigations

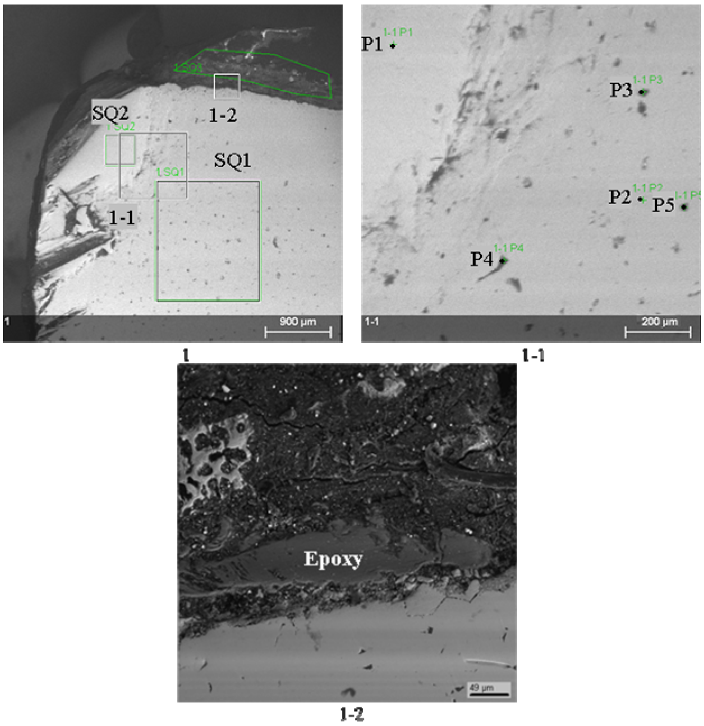

1 1-1

1-2

Fig. 2.16 – Micrographs of area 1

Table 2.8 –EDX data on area 1

No.		Fe	Mn	Mo	Si	Ni	Cr	O	Phase
SQ1	mass %	96.0	1.8	0.6	0.3	1.1	0.3	-	steel
	mol. %	95.9	1.8	0.3	0.6	1.0	0.3	-	
SQ2	mass %	96.2	1.6	0.6	0.3	1.1	0.3	-	
	mol. %	96.2	1.6	0.4	0.5	1.0	0.3	-	
P1	mass %	96.5	1.9	0.3	0.1	1.0	0.4	-	
	mol. %	96.5	1.9	0.2	0.1	0.9	0.4	-	
P2	mass %	96.9	1.5	0.3	0.2	0.9	0.3	-	
	mol. %	96.8	1.6	0.2	0.3	0.8	0.3	-	
P3	mass %	96.6	1.6	0.3	0.2	0.9	0.3	-	
	mol. %	96.5	1.6	0.2	0.5	0.9	0.3	-	
P4	mass %	96.0	1.7	0.5	0.2	1.3	0.4	-	
	mol. %	96.1	1.7	0.3	0.4	1.2	0.4	-	
P5	mass %	93.7	1.9	0.7	0.4	1.2	0.3	-	
	mol. %	89.5	1.9	0.4	0.8	1.1	0.3	-	
	mol. % MeO_x	95.3	2.0	0.4	0.8	1.2	0.3	▨	
P6	mass %	92.3	1.6	1.0	0.7	1.2	0.4	-	
	mol. %	86.0	1.5	0.6	1.3	1.1	0.4	-	
	mol. % MeO_x	94.7	1.7	0.6	1.4	1.2	0.4	▨	
P7	mass %	96.5	1.7	0.5	0.4	0.7	0.2	-	
	mol. %	96.3	1.7	0.3	0.8	0.7	0.2	-	

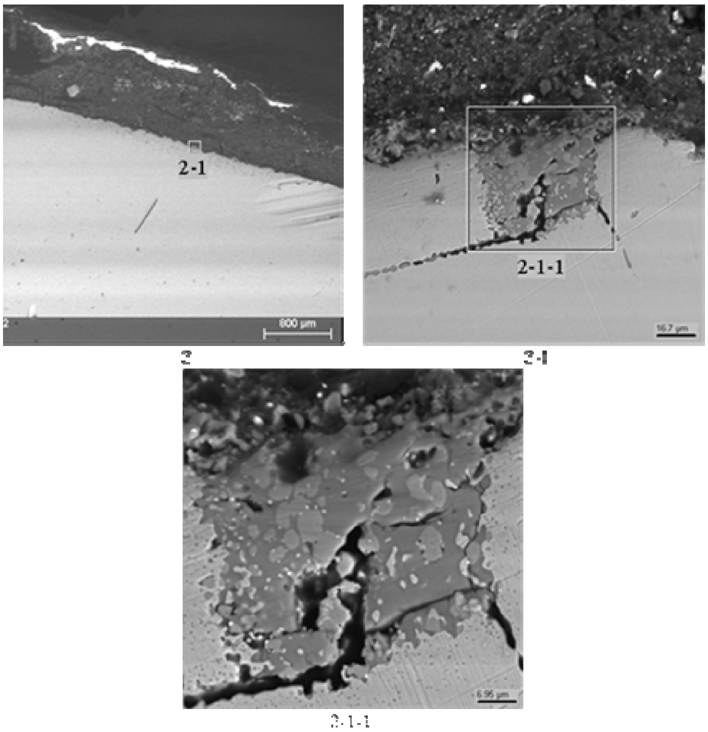

Fig. 2.17 – Micrographs of area 2.

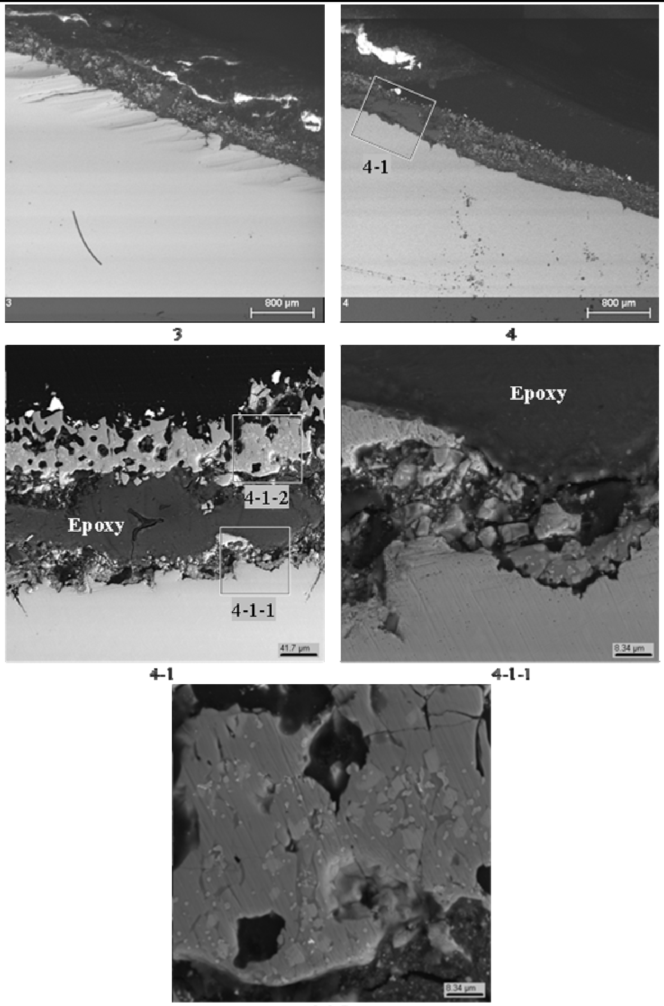

3 4

4-1 4-1-1

4-1-2

Fig. 2.18 – Micrographs of areas 3 and 4.

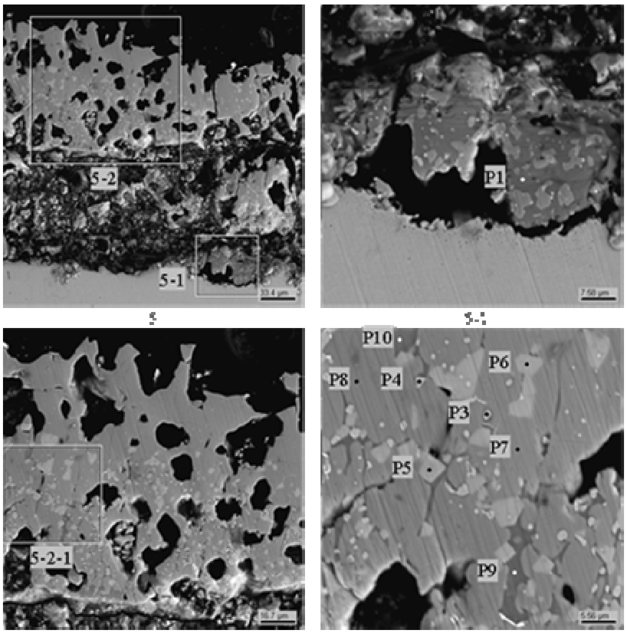

5 5-1

5-2 5-2-1

Fig. 2.19 – Micrographs of area 5.

Table 2.9 – EDX data on area 5

No.		U	Zr	Fe	Mn	Mo	Si	Ni	Cr	O	Phase
P1	mass %	-	0.4	41.4	1.9	0.1	15.7	0.2	-	40.3	Fayalite Fe_2SiO_4
	mol. %	-	0.1	19.2	0.9	<0.1	14.5	0.1	-	65.2	
	mol. % MeO_x	-	0.3	55.2	2.6	0.1	41.7	0.2	-		
P2	mass %	7.7	7.8	0.2	55.5	2.9	0.1	8.8	0.6	23.9	
	mol. %	1.1	1.1	0.1	34.2	1.8	0.0	10.8	0.3	51.4	
	mol. % MeO_x	2.3	2.3	0.1	70.4	3.8	0.1	22.2	0.7		
P3	mass %	0.5	-	46.2	0.8	4.4	1.2	34.7	0.4	11.9	γ-(Fe,Ni)
	mol. %	0.1	-	36.5	0.6	2.0	1.9	26.0	0.3	32.7	
	mol. % MeO_x	0.1	-	54.1	0.9	3.0	2.9	38.6	0.5		
P4	mass %	0.6	-	48.8	0.9	1.4	2.2	32.0	-	13.7	
	mol. %	0.1	-	36.5	0.7	0.6	3.3	22.8	-	35.9	
	mol. % MeO_x	0.2	-	56.9	1.1	1.0	5.1	35.5	-		
P5	mass %	-	0.3	49.9	0.8	23.3	0.1	2.8	1.2	21.6	Presumably Fe_3MoO_4 [14]
	mol. %	-	0.1	34.6	0.6	9.4	0.2	1.8	0.9	52.4	
	mol. % MeO_x	-	0.3	72.7	1.2	19.8	0.4	3.8	1.9		
P6	mass %	0.3	0.2	47.4	0.7	24.1	0.4	2.1	1.3	23.5	
	mol. %	0.1	0.1	31.9	0.5	9.4	0.6	1.4	1.0	55.2	
	mol. % MeO_x	0.1	0.1	71.3	1.1	21.1	1.2	3.0	2.2		
P7	mass %	0.5	0.0	74.4	1.1	0.3	0.2	2.0	0.5	21.0	$Fe_{1-x}O$
	mol. %	0.1	0.0	48.9	0.7	0.1	0.3	1.3	0.4	48.3	
	mol. % MeO_x	0.1	0.0	94.5	1.4	0.2	0.5	2.5	0.7		
P8	mass %	-	-	76.9	1.3	-	0.1	1.7	0.5	19.4	
	mol. %	-	-	51.8	0.9	-	0.2	1.1	0.4	45.7	
	mol. % MeO_x	-	-	95.4	1.7	-	0.3	2.0	0.7		
P9	mass %	-	0.2	53.2	3.4	0.2	12.5	1.0	0.2	29.3	Fayalite Fe_2SiO_4
	mol. %	-	0.1	28.7	1.9	0.1	13.4	0.5	0.1	55.2	
	mol. % MeO_x	-	0.1	64.2	4.2	0.2	30.0	1.1	0.3		
P10	mass %	1.3	0.3	54.1	3.1	0.2	12.4	0.9	0.3	27.5	
	mol. %	0.2	0.1	30.1	1.8	0.1	13.7	0.5	0.2	53.4	
	mol. % MeO_x	0.4	0.2	64.7	3.8	0.1	29.5	1.0	0.4		

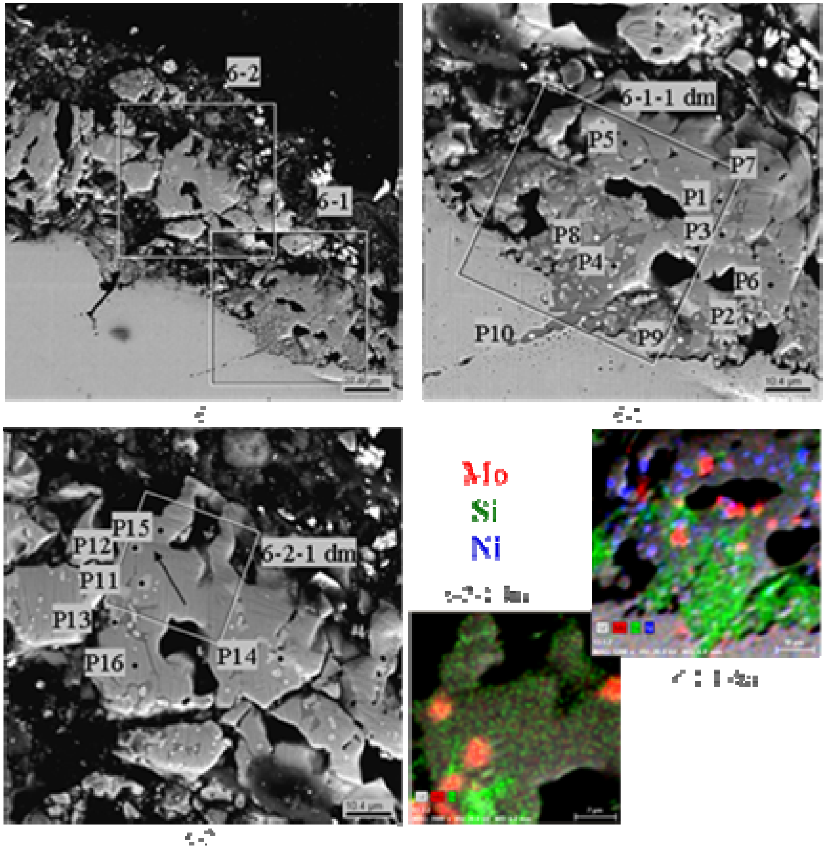

Fig. 2.20 – Micrographs of area 6
(with X-ray mapping of the chosen zones)

Table 2.10 – EDX data on area 6

№		U	Zr	Fe	Mn	Mo	Si	Ni	Cr	O	Phase
P1	mass.%	1.1	-	65.0	1.0	2.8	5.7	5.6	0.2	18.6	γ-(Fe,Ni)
	mol.%	0.2	-	43.4	0.7	1.1	7.6	3.6	0.2	43.4	
	mol.% MeO_x	0.3	-	76.6	1.2	1.9	13.3	6.3	0.3		
P2	mass.%	0.5	0.4	58.7	1.7	1.1	11.9	2.2	-	23.5	
	mol.%	0.1	0.1	34.7	1.0	0.4	14.0	1.3	-	48.5	
	mol.% MeO_x	0.1	0.3	67.4	1.9	0.7	27.1	2.4	-		
P3	mass %	0.6	-	64.1	1.0	2.7	8.3	4.7	-	18.6	
	mol.%	0.1	-	41.9	0.7	1.0	10.8	2.9	-	42.5	
	mol.% MeO_x	0.2	-	73.1	1.2	1.8	18.8	5.1	-		
P4	mass.%	0.4	0.3	66.8	0.8	2.5	7.8	3.8	-	17.7	
	mol.%	0.1	0.1	44.5	0.5	1.0	10.3	2.4	-	41.1	
	mol.% MeO_x	0.1	0.2	75.6	0.9	1.6	17.5	4.0	-		
P5	mass.%	-	0.3	66.2	0.7	0.4	0.7	0.3	0.2	31.4	$Fe_{1-x}O$
	mol.%	-	0.1	37.0	0.4	0.1	0.8	0.2	0.1	61.3	
	mol.% MeO_x	-	0.3	95.8	1.0	0.3	2.0	0.4	0.4		
P6	mass.%	1.0	-	64.9	0.9	0.4	0.3	0.4	0.4	31.7	
	mol.%	0.1	-	36.4	0.5	0.1	0.4	0.2	0.2	62.0	
	mol.% MeO_x	0.3	-	95.8	1.3	0.4	1.0	0.6	0.6		
P7	mass.%	0.5	-	69.7	0.8	0.4	0.6	0.5	0.3	27.3	
	mol.%	0.1	-	41.5	0.5	0.1	0.7	0.3	0.2	56.7	
	mol.% MeO_x	0.2	-	95.8	1.1	0.3	1.7	0.7	0.4		
P8	mass.%	-	-	51.6	2.2	0.1	14.7	0.4	0.1	30.9	Fayalite Fe_2SiO_4
	mol.%	-	-	26.8	1.2	0.0	15.3	0.2	0.1	56.5	

№		U	Zr	Fe	Mn	Mo	Si	Ni	Cr	O	Phase
	.% MeO_x	-	-	61.6	2.7	0.1	35.0	0.5	0.1		
P9	mass.%	-	-	50.3	2.2	0.3	14.6	0.6	-	32.0	
	mol.%	-	-	25.9	1.2	0.1	15.0	0.3	-	57.6	
	mol.% MeO_x	-	-	61.1	2.7	0.2	35.2	0.7	-		
P10	mass.%	-	-	57.7	1.7	0.4	10.7	0.9	0.2	28.5	
	mol.%	-	-	31.8	0.9	0.1	11.7	0.4	0.1	54.8	
	mol.% MeO_x	-	-	70.4	2.1	0.3	26.0	1.0	0.3		
P11	mass.%	0.7	0.2	47.0	0.8	24.8	0.2	0.7	1.6	24.2	Presumably Fe_3MoO_4
	mol.%	0.1	0.1	31.5	0.6	9.7	0.2	0.4	1.1	56.4	
	mol.% MeO_x	0.3	0.2	72.2	1.3	22.2	0.5	1.0	2.6		
P12	mass.%	0.6	0.2	49.4	0.8	22.4	0.8	0.8	1.3	23.8	
	mol.%	0.1	0.1	32.9	0.5	8.7	1.0	0.5	0.9	55.3	
	mol.% MeO_x	0.2	0.2	73.6	1.2	19.4	2.3	1.1	2.1		
P13	mass.%	-	0.4	45.9	0.6	26.3	0.2	0.4	1.6	24.5	
	mol.%	-	0.2	30.4	0.4	10.2	0.3	0.3	1.2	57.0	
	mol.% MeO_x	-	0.3	70.9	1.0	23.7	0.7	0.7	2.7		
P14	mass.%	-	0.2	50.6	0.7	19.6	0.2	0.3	1.2	27.4	
	mol.%	-	0.1	31.4	0.4	7.1	0.2	0.2	0.8	59.8	
	mol.% MeO_x	-	0.2	78.2	1.1	17.7	0.5	0.4	2.0		
P15	mass.%	-	-	68.1	0.9	-	0.6	0.3	-	28.8	$Fe_{1-x}O$
	mol.%	-	-	39.6	0.5	-	0.7	0.2	-	58.4	
	mol.% MeO_x	-	-	95.3	1.2	-	1.7	0.4	-		
P16	mass.%	-	-	70.2	1.0	-	0.4	0.6	-	25.4	
	mol.%	-	-	43.1	0.7	-	0.5	0.3	-	54.4	
	mol.% MeO_x	-	-	94.6	1.4	-	1.1	0.7	-		

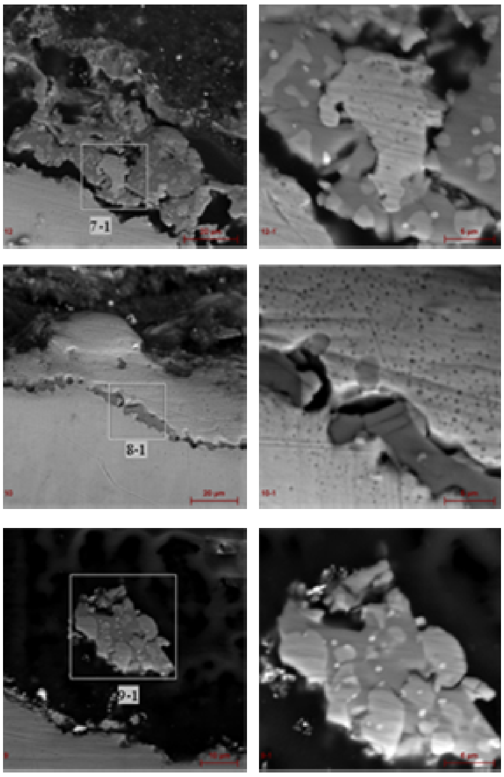

Fig. 2.21 – Micrographs of areas 7-9

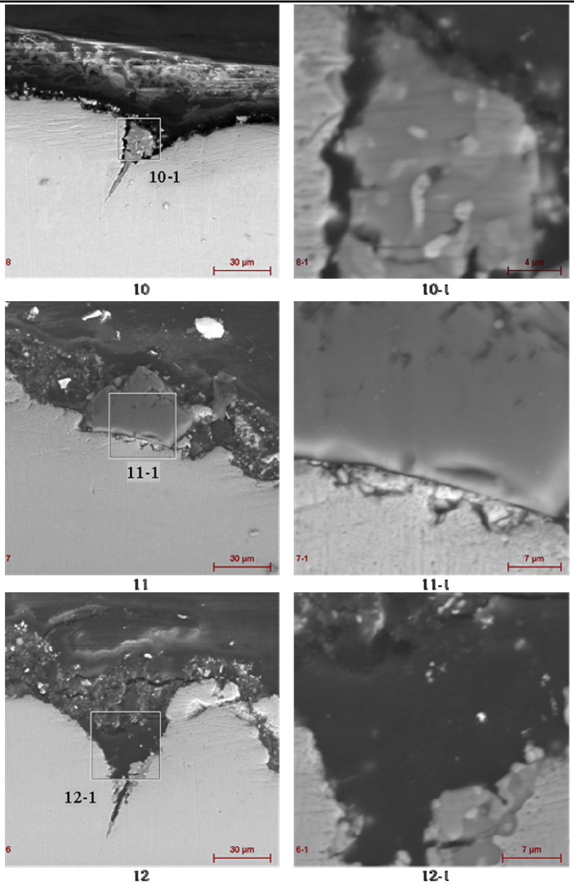

Fig. 2.22 – Micrographs of areas 10-12

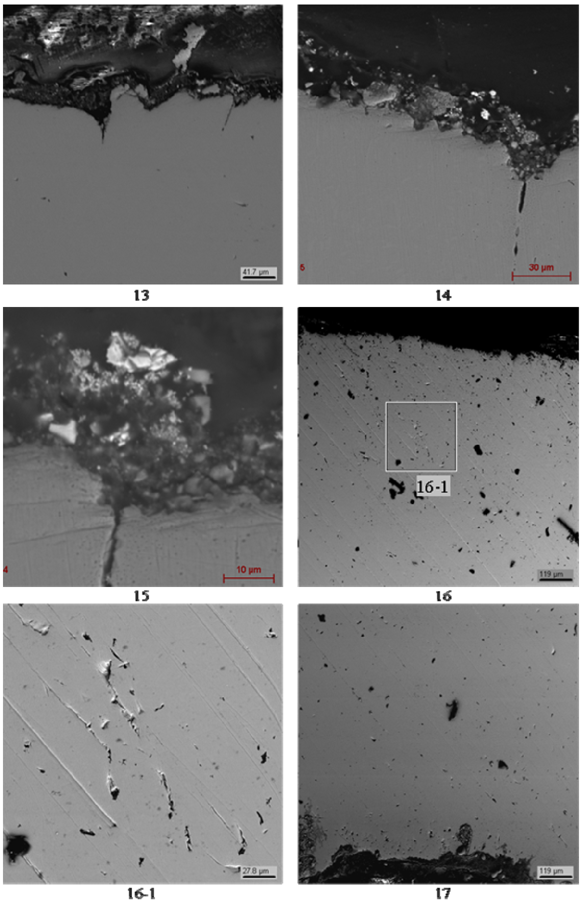

Fig. 2.23 – Micrographs of areas 13-17

Fig. 2.24 shows a polished section from an ingot fragment that separated from the steel specimen during the furnace disassembly. The results of SEM/EDX analysis of the marked areas are presented in Figs. 2.25-2.31 and Tabs. 2.12-2.17.

In the lower part immediately adjacent to steel, there is a dense layer composed predominantly of the wustite-based phase along the entire polished section. Boundary of this layer is clearly outlined from both the sides of steel and oxidic melt, thus being an evidence in favour of the established stable-state structure of the corrosion front. Thickness of this layer remains the same across the entire polished section and equals ~300 µm. The layer composition (in mol. %) is 0.5±0.2 Zr, 41.9±0.8 Fe, 0.7±0.1 Mn, 0.5±0.3 Ni, 56.1±0.8 O (statistics for 7 areas with uniform structure of wustite with thin intergrain veins). The central part of the layer shows microstructure irregularities (eutectic crystallization zones, Fig. 2.27, area 2-1-2; $(U,Zr)O_2$–based solid solution grains, Fig. 2.30, area 5-1), which are most likely due to a rate of this layer formation that is higher than those in the peripheral areas (Fig. 2.30). It is here that the boundary between the melt and a wustite layer is most fuzzy, and a highly porous layer of wustite is present from the side of the steel. Thus, it can be concluded that microstructure in this zone in the least corresponds to the stable-state condition and to the greatest extent has been distorted by the interaction kinetics.

Crystallized corium is found above the wustite layer (e.g., Fig. 2.26). The absence of a shrinkage crack between the wustite layer and crystallized melt, as well as the presence of rounded pores with a characteristic size from 0.2 to 0.5 mm (Fig. 2.31) should be noted. Also, it should be noted that the crystallized corium near the wustite layer is somewhat enriched in the refractory component. These facts evidence that the melt was located immediately above the wustite layer during the test and crystallized when the induction heating has been disconnected. The enriched zone is not solid. The main phase of corium is the dendritically crystallized UO_2,ZrO_2(FeO)–based solid solution that changes the U:Zr ratio from the dendrite center (enriched in Zr) to the periphery (enriched in U) (Fig. 2.28, area 3-2, Fig. 2.29). Zones of eutectic crystallization are observed between dendrites. Tab. 2.11 offers the generalized data on the bulk corium and eutectics composition.

Table 2.11 – EDX data on the composition of bulk corium and eutectics

Phase		U	Zr	Fe	Ni	O
Corium (6 fields)	mass %	33.6±1.6	14.6±1.7	22.8±0.4	0.6±0.3	28.4±0.5
	mol. %	5.7±0.3	6.4±0.8	16.4±0.3	0.4±0.2	71.0±0.8
	mol. % MeO_x	19.6±1.4	22.1±2.1	56.7±1.3	1.3±0.6	
Corium enriched in refractory component (5 fields)	mass %	35.1±4.4	20.0±4.4	17.6±0.3	0.3±0.3	26.9±0.4
	mol. %	6.2±0.9	9.2±1.9	13.3±0.3	0.2±0.2	71.0±0.5
	mol. % MeO_x	21.5±3.6	31.7±6.1	45.7±1.8	0.7±0.7	
Eutectics (4 fields)	mass %	23.4±0.2	4.6±0.3	42.2±1.9	0.6±0.1	28.9±1.6
	mol. %	3.6±0.1	1.8±0.1	27.8±1.9	0.4±0.1	66.2±2.0
	mol. % MeO_x	10.7±0.4	5.5±0.5	82.2±0.7	1.1±0.2	

It should be noted that composition of eutectic zones does not correspond to the eutectic composition of either the $FeO–UO_2–ZrO_2$ system (in mol. %: 91.8±0.5 FeO, 3.8±0.3 UO_2, 4.4±0.4 ZrO_2, eutectic temperature of 1310±5°C) [15] or the $Fe_2O_3–U_3O_8–ZrO_2$ system (in mol.: %: 67.4±1.0 $FeO_{1.5}$, 30.5±1.0 UO_2, 2.1±0.2 ZrO_2, eutectic temperature of 1323±7°C) [16] and is most close to the composition calculated with the GEMINI2 code [17] on the basis of NUCLEAiv-10.1 database [18] (in mol.: %: 80.8 $FeO_{1.5}$, 10.7 UO_2, 8.4 ZrO_2, eutectic temperature 1396±1°C). A possible reason may be that temperature conditions during MCP-4 and the oxygen partial pressure in the system facilitated the existence and crystallization of iron oxide in the form of Fe_3O_4. Both the code and database have also been optimized for these conditions.

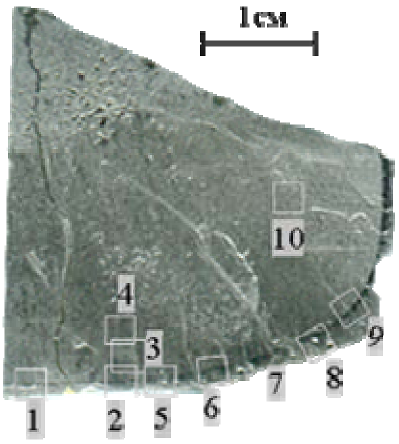

Fig. 2.24 – Polished section of the ingot from MCP-4 with areas marked for SEM/EDX investigation

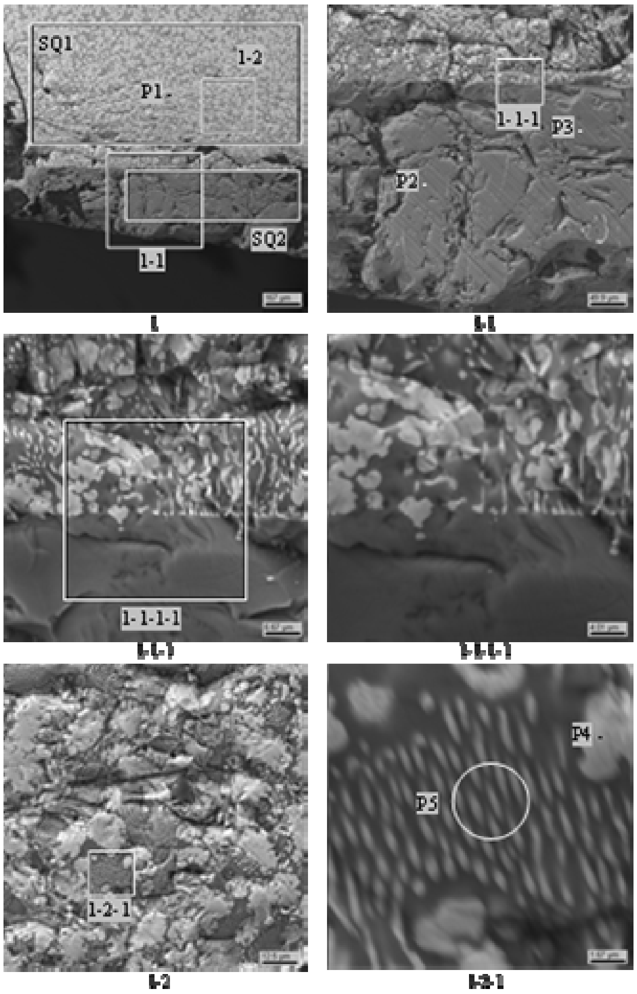

Fig. 2.25 – Micrograph of area 1

Table 2.12 – EDX data on area 1

No.		U	Zr	Fe	Mn	Ni	O	Phase
SQ1	mass %	26.4	9.8	32.7	-	0.7	30.5	
	mol. %	4.1	4.0	21.5	-	0.4	70.0	
	mol. % MeO_x	13.6	13.3	71.7	-	1.4		
SQ2	mass %	-	0.7	71.3	1.4	0.7	25.9	~$Fe_{1-x}O$
	mol. %	-	0.3	43.3	0.9	0.4	55.1	
	mol. % MeO_x	-	0.6	96.5	1.9	1.0		
P1	mass %	15.0	4.7	63.4	-	-	16.9	Mixture of phases
	mol. %	2.7	2.2	49.2	-	-	45.9	
	mol. % MeO_x	5.0	4.1	90.9	-	-		
P2	mass %	-	-	75.9	-	-	24.1	$Fe_{1-x}O$
	mol. %	-	-	47.4	-	-	52.6	
	mol. % MeO_x	-	-	100	-	-		
P3	mass %	-	-	72.3	-	-	27.7	
	mol. %	-	-	42.8	-	-	57.2	
	mol. % MeO_x	-	-	100	-	-		
P4	mass %	59.7	22.2	6.5	-	-	11.6	$(U,Zr,Fe)O_2$
	mol. %	18.8	18.3	8.8	-	-	54.2	
	mol. % MeO_x	41.0	39.9	19.1	-	-		
P5	mass %	24.7	6.4	46.5	-	-	22.4	Eutectics
	mol. %	4.3	2.9	34.6	-	-	58.2	
	mol. % MeO_x	10.3	6.9	82.8	-	-		

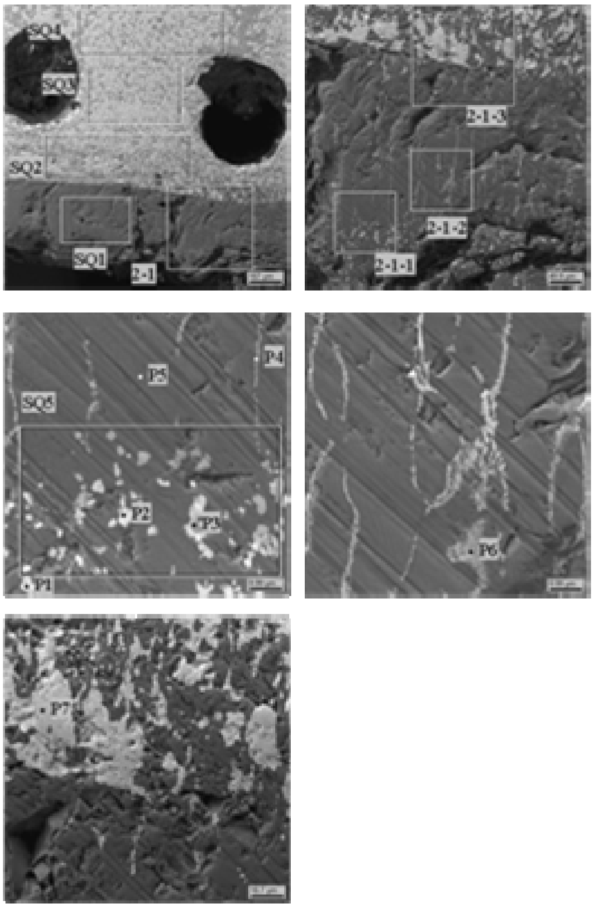

Fig. 2.26 – Micrographs of area 2

Table 2.13 – EDX data on area 2

No.		U	Zr	Fe	Mn	Ni	O	Phase
SQ1	mass %	-	1.6	69.1	1.1	-	27.4	-
	mol. %	-	0.6	41.4	0.7	-	57.2	
	mol. % MeO_x	-	1.4	96.7	1.6	-		
SQ2	mass %	36.4	11.5	22.6	-	-	29.3	-
	mol. %	6.1	5.0	16.1	-	-	72.7	
	mol. % MeO_x	22.3	18.4	59.0	-	-		
SQ3	mass %	35.7	20.1	17.2	-	-	27.0	-
	mol. %	6.3	9.3	13.0	-	-	71.3	
	mol. % MeO_x	22.1	32.4	45.3	-	-		
SQ4	mass %	31.4	23.5	17.8	-	-	27.2	-
	mol. %	5.5	10.7	13.3	-	-	70.5	
	mol. % MeO_x	18.5	36.2	44.9	-	-		
SQ5	mass %	7.5	3.2	59.5	0.9	0.7	28.2	-
	mol. %	1.1	1.2	36.4	0.6	0.4	60.3	
	mol. % MeO_x	2.7	3.0	91.9	1.4	1.0		
P1	mass %	68.3	5.2	5.7	-	0.5	20.2	$(U,Zr,Fe)O_2$
	mol. %	16.7	3.3	5.9	-	0.5	73.5	
	mol. % MeO_x	62.9	12.4	22.3	-	1.7		
P2	mass %	45.3	5.2	24.3	0.3	0.6	24.2	$(U,Zr,Fe)O_2$
	mol. %	8.6	2.6	19.7	0.3	0.5	68.4	
	mol. % MeO_x	27.2	8.2	62.3	0.8	1.6		
P3	mass %	51.2	10.2	14.9	-	0.5	23.0	Eutectics
	mol. %	10.5	5.5	13.0	-	0.4	70.4	
	mol. % MeO_x	35.5	18.5	44.0	-	1.3		
P4	mass %	-	-	73.0	1.4	0.6	24.3	Intergrain diffusion
	mol. %	-	-	45.6	0.9	0.4	53.1	
	mol. % MeO_x	-	-	97.1	1.9	0.8		
P5	mass %	-	-	73.8	1.4	0.8	23.2	FeO
	mol. %	-	-	46.9	0.9	0.5	51.6	
	mol. % MeO_x	-	-	96.9	1.9	0.9		
P6	mass %	34.8	18.7	23.5	0.7	-	22.3	Eutectics
	mol. %	6.7	9.4	19.4	0.5	-	64.0	
	mol. % MeO_x	18.6	26.1	53.7	1.5	-		
P7	mass %	63.3	12.6	4.7	0.2	0.5	18.6	$(U,Zr,Fe)O_2$
	mol. %	16.0	8.3	5.0	0.3	0.6	69.9	
	mol. % MeO_x	53.0	27.6	16.7	0.9	1.9		

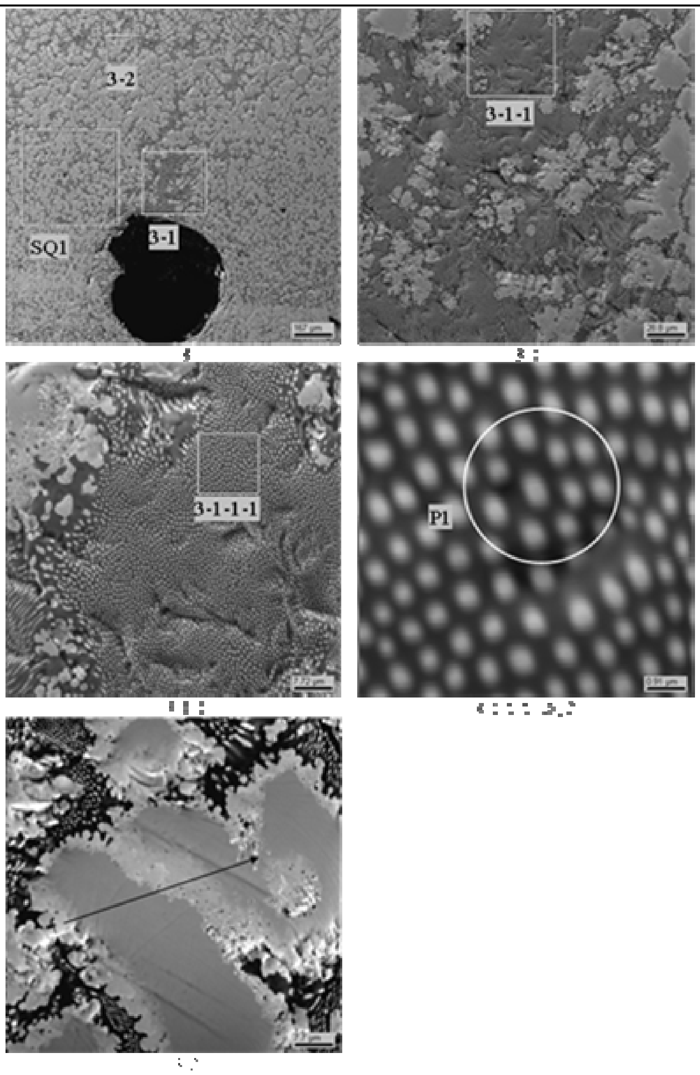

Fig. 2.27 – Micrographs of area 3

Table 2.14 – EDX data on area 3

No.		U	Zr	Fe	Ni	O	Phase
SQ2	mass %	23.4	4.5	41.5	0.6	29.6	eutectics
	mol. %	3.6	1.8	26.9	0.4	67.1	
	mol. % MeO_x	10.8	5.5	82.0	1.2		
P1	mass %	23.5	5.0	40.0	0.5	30.8	
	mol. %	3.5	1.9	25.5	0.3	68.6	
	mol. % MeO_x	11.2	6.2	81.2	0.9		

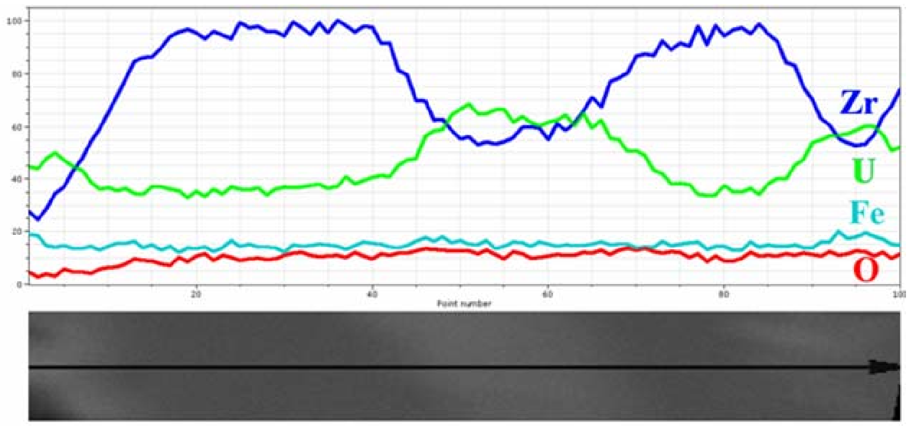

Fig. 2.28 – Concentration profile of the $(U,Zr)O_2$ solid solution grains aggregate along the direction marked in Fig. 2.27

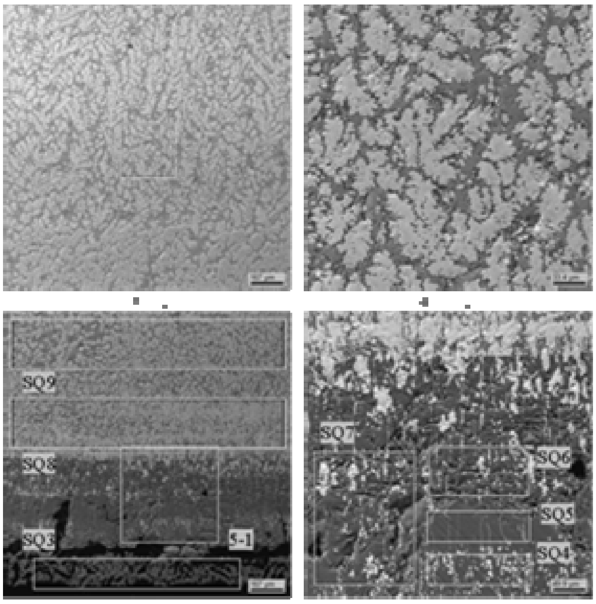

Fig. 2.29 – Micrograph of areas 4 and 5

Table 2.15 – EDX data on areas 4 and 5

No		U	Zr	Fe	Mn	Ni	O
SQ1	mass %	32.9	15.8	22.6	-	0.6	28.0
	mol. %	5.6	7.0	16.3	-	0.4	70.6
	mol. % MeO_x	19.0	23.8	55.5	-	1.5	
SQ2	mass %	32.3	15.3	23.4	-	0.7	28.2
	mol. %	5.4	6.7	16.8	-	0.5	70.6
	mol. % MeO_x	18.4	22.8	57.0	-	1.6	
SQ3	mass %	-	2.0	68.0	1.1	1.5	26.1
	mol. %	-	0.8	41.7	0.7	0.9	55.8
	mol. % MeO_x	-	1.7	94.3	1.6	2.0	
SQ4	mass %	6.8	2.4	60.2	1.0	0.7	28.9
	mol. %	1.0	0.9	36.3	0.6	0.4	60.8
	mol. % MeO_x	2.4	2.3	92.6	1.6	1.0	
SQ5	mass %	2.2	2.4	66.7	1.1	0.6	27.0
	mol. %	0.3	0.9	40.5	0.7	0.3	57.3
	mol. % MeO_x	0.8	2.1	94.8	1.5	0.8	
SQ6	mass %	10.5	4.0	53.6	0.6	0.7	30.6
	mol. %	1.5	1.5	32.1	0.4	0.4	64.2
	mol. % MeO_x	4.1	4.1	89.6	1.1	1.1	
SQ7	mass %	6.8	3.3	59.2	0.9	0.7	29.2
	mol. %	1.0	1.2	35.6	0.5	0.4	61.4
	mol. % MeO_x	2.5	3.2	92.1	1.4	1.0	
SQ8	mass %	42.2	13.1	17.7	-	0.7	26.2
	mol. %	7.7	6.3	13.8	-	0.5	71.6
	mol. % MeO_x	27.2	22.0	48.5	-	1.8	
SQ9	mass %	34.4	14.1	22.8	-	0.7	28.0
	mol. %	5.8	6.2	16.6	-	0.5	70.8
	mol. % MeO_x	20.0	21.4	56.7	-	1.6	

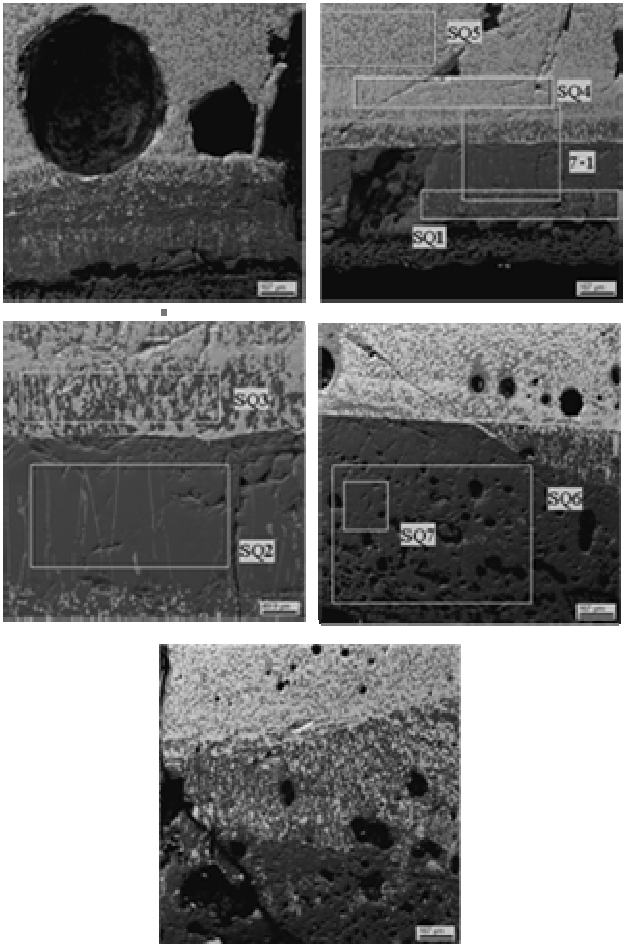

Fig. 2.30 – Micrographs of areas 6-9

Table 2.16 – EDX data on areas 7 and 8

No		U	Zr	Fe	Mn	Si	Ni	Cr	O
SQ1	mass %	8.7	3.4	57.0	0.8	-	0.8	-	29.3
	mol. %	1.2	1.3	34.6	0.5	-	0.4	-	62.0
	mol. % MeO_x	3.3	3.4	90.9	1.4	-	1.2	-	
SQ2	mass %	1.1	1.5	68.8	1.1	-	0.6	-	26.8
	mol. %	0.2	0.6	41.6	0.7	-	0.4	-	56.6
	mol. % MeO_x	0.3	1.3	95.9	1.6	-	0.8	-	
SQ3	mass %	25.2	8.7	34.9	-	-	0.8	-	30.1
	mol. %	3.9	3.5	22.9	-	-	0.5	-	69.0
	mol. % MeO_x	12.5	11.3	74.0	-	-	1.5	-	
SQ4	mass %	46.5	19.1	9.3	-	-	0.6	-	24.5
	mol. %	9.3	9.9	7.9	-	-	0.5	-	72.4
	mol. % MeO_x	33.6	35.9	28.5	-	-	1.6	-	
SQ5	mass %	34.8	19.2	17.9	-	-	0.8	-	27.2
	mol. %	6.1	8.8	13.4	-	-	0.5	-	71.1
	mol. % MeO_x	21.2	30.4	46.2	-	-	1.9	-	
SQ6	mass %	-	0.8	68.7	1.0	0.6	1.1	0.5	26.4
	mol. %	-	0.3	41.6	0.6	0.8	0.6	0.3	55.7
	mol. % MeO_x	-	0.7	93.9	1.4	1.7	1.4	0.7	
SQ7	mass %	-	-	69.7	1.2	-	1.1	-	26.2
	mol. %	-	-	42.3	0.7	-	0.6	-	55.6
	mol. % MeO_x	-	-	95.2	1.7	-	1.5	-	

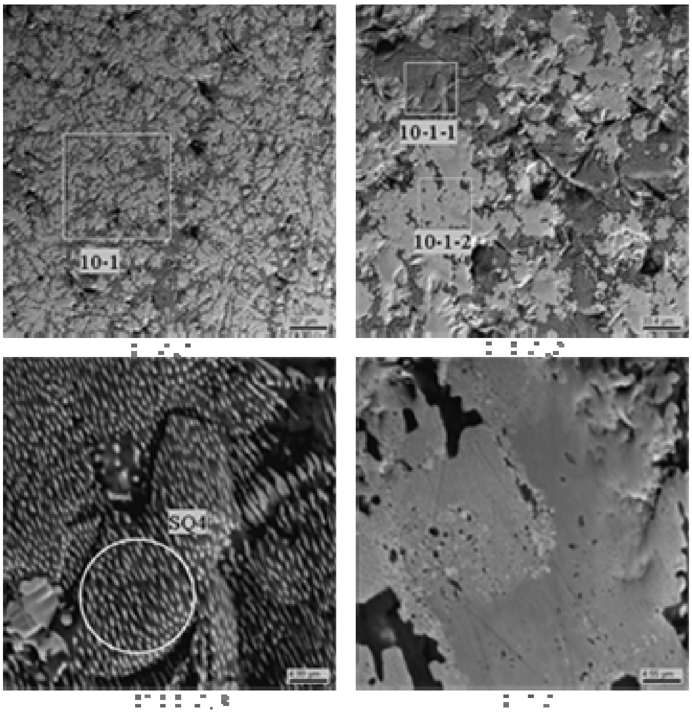

Fig. 2.31 – Micrographs of area 10

Table 2.17 – EDX data on area 10

No.		U	Zr	Fe	Ni	O	Phase
SQ3	mass %	23.4	4.5	43.2	0.7	28.1	eutectics
	mol. %	3.7	1.8	28.8	0.4	65.2	
	mol. % MeO_x	10.5	5.2	82.6	1.2		
SQ4	mass %	23.1	4.4	44.2	0.7	27.2	
	mol. %	3.7	1.8	29.8	0.5	64.0	
	mol. % MeO_x	10.2	5.1	82.9	1.3		

It should also be noted that the composition of square SQ6 in zone 5-1 (Fig. 2.29, zone 5-1, Tab. 2.15) corresponds quite precisely to the eutectic composition of the FeO-UO_2-ZrO_2 system (according to CORPHAD data, the temperature of said eutectics crystallization is 1310±5°C). Therefore, the temperature in this zone should be below 1310°C. Most likely, said zone (SQ6) was in liquid state at a transient stage of the test, and the observed structure has resulted from annealing, i.e., recrystallization of the crystallized eutectics. At the same time, zone SQ5 right below SQ6 showed no traces of the liquid phase. The width of this zone in the narrowest place (which is presented in Fig. 2.29) is about 50 µm.

A comparative analysis of microstructures and compositions for MC12 and MCP-4 (the tests with more or less similar experimental conditions) is given below.

Notable is that the general view (Fig. 2.32) shows large pores concentrated along the boundary between the iron oxide layer and the crystallized melt (because of the gas bubbles formation on the iron oxide surface).

In MC12, zones with a clearly expressed crystallization of eutectic type are present in the wustite layer at the boundary with corium (Fig. 2.33). Composition of these zones (Tab. 2.18) is quite close to that of the eutectics in the FeO-UO_2-ZrO_2 system. Such zones are absent in MCP-4. However, the bulk composition of the wustite layer upper part with inclusions in the central part of the ingot corresponds to the eutectic composition (Tab. 2.15, SQ6). Therefore, the oxygen potential of the system in the considered zone corresponds to the equilibrium iron crystallization in the form of wustite, while in the above-located areas (in the corium zone) the oxygen potential is changing.

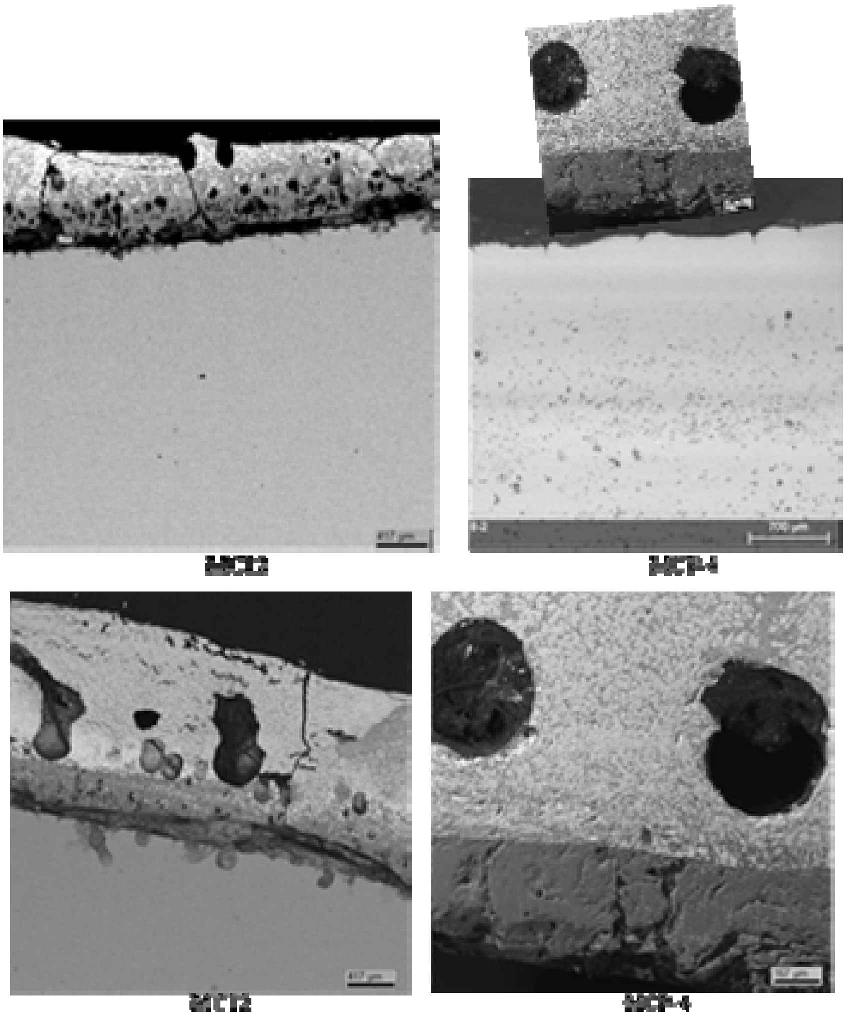

Fig. 2.32 – General view of the corrosion layer structure in MC12 and MPC-4

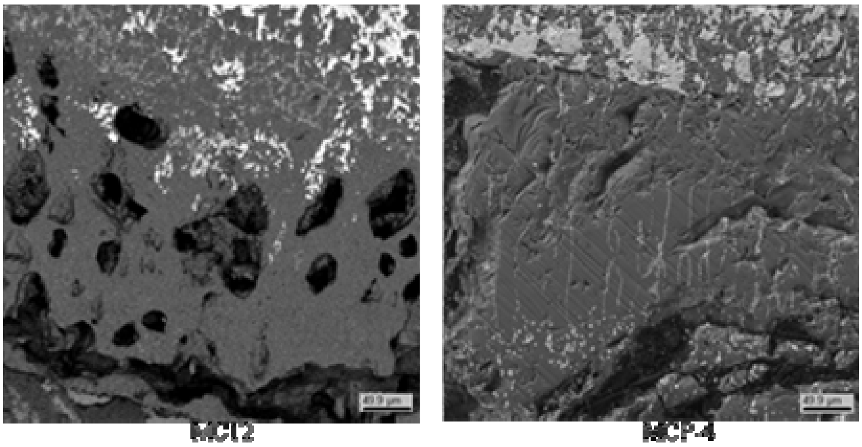

Fig. 2.33 – Corrosion layer microstructure at the ‘iron oxide/corium’ boundary in MC12 and MPC-4

Table 2.18 – EDX data on the eutectic areas at the 'iron oxide/corium' boundary in MC12

No.	U	Zr	Fe	Cr	Ni	Mn	Si	Mo	~O
Eutectics, mol. %	3.3±1.3	2.0±0.7	41.7±2.2	1.1±1.0	0.3±0.2	0.07±0.06	0.3±0.05	-	51.2±1.7
mol. % MeO$_x$	6.7	4.2	85.5	2.2	0.7	0.1	0.6	-	

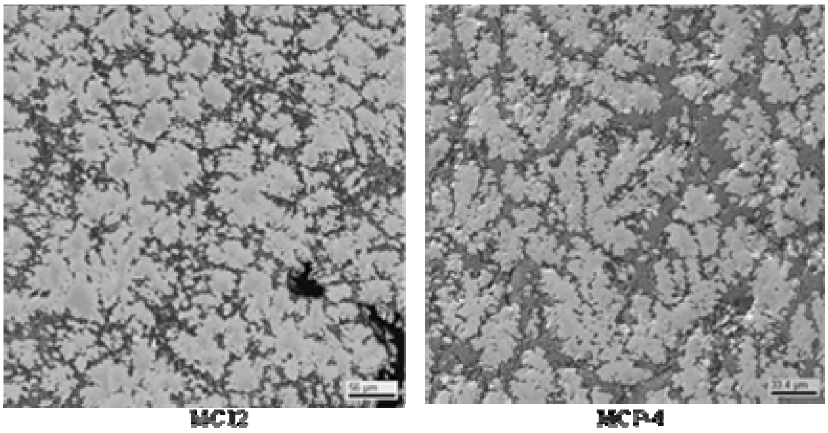

MC12 MCP-4

Fig. 2.34 – Corium microstructure in MC12 and MPC-4

Table 2.19 – EDX data on corium composition in MC12 and MCP-4

		U	Zr	Fe	Si	~O
MC12	mass %	34.0	14.9	19.9	0.2	31.0
	mol. %	6.7±1.1	7.2±1.1	15.8±2.1	0.3±0.1	69.9±4.4
	mol. % MeO$_x$	22.4	24.1	52.6	0.9	

		U	Zr	Fe	Ni	O
MCP-4	mass %	33.6±1.6	14.6±1.7	22.8±0.4	0.6±0.3	28.4±0.5
	mol. %	5.7±0.3	6.4±0.8	16.4±0.3	0.4±0.2	71.0±0.8
	mol. % MeO$_x$	19.6±1.4	22.1±2.1	56.7±1.3	1.3±0.6	

Corium microstructure and composition (Fig. 2.34) are sufficiently similar in both tests (Tab. 2.19), as well as the eutectic zones in corium (Tab. 2.20). It means that the oxygen potential at the ingot crystallization stage corresponded to the conditions of one and the same form of iron oxide.

Table 2.20 – EDX data on the composition of corium eutectic zones in MC12 and MCP-4

No.		U	Zr	Fe	Cr	Ni	Si	~O
Eutectics MC12	mass %	25.9	5.9	49.8	0.1	0.3	0.2	17.7
	mol. %	5.0	3.0	40.8	0.1	0.3	0.3	50.6
	mol. % MeO$_x$	10.1	6.0	82.6	0.2	0.5	0.5	

		U	Zr	Fe	Ni	O
Eutectics MCP-4	mass %	23.4±0.2	4.6±0.3	42.2±1.9	0.6±0.1	28.9±1.6
	mol. %	3.6±0.1	1.8±0.1	27.8±1.9	0.4±0.1	66.2±2.0
	mol. % MeO$_x$	10.7±0.4	5.5±0.5	82.2±0.7	1.1±0.2	

So, it may be concluded that the boundary character in both tests is generally similar. However, the iron oxide at the metal/oxide boundary in MCP-4 is denser than in MC12. This oxidic layer broke off from the side of the metal instead of that of oxides. In addition to fayalite, a phase that corresponds to Fe_3MoO_4 has been discovered at the boundary with metal. The presence of this phase is determined by the big amount of molybdenum in the European steel. It may be supposed that this phase has little effect on the interaction front, since quantity of this phase is small and, like in MC12, fayalite is concentrated along the boundary. An important peculiarity of the interaction zone in MCP-4 is the presence of a clearly expressed ‘iron oxide/melt’ boundary across the entire analyzed polished section (a transition from the wustite crust to the oxidic part is sharp and contains no turbulences and droplet zones enriched in iron). Such a boundary was missing in MC12. Also, the wustite zone in MCP-4 does not contain noticeable quantities of silicon and eutectic crystallization areas, as it was the case in MC12. No disturbance of the iron oxide layer completeness was found in MCP-4, unlike in MC12.

3 DISCUSSION OF RESULTS

The works [1, 2] describe a model that was used for generalizing experimental data on the VVER vessel steel corrosion at the interaction with molten corium in the oxidizing atmosphere. The model is based on the Tamman’s equation [13] and supposes that the main obstacle for Fe^{2+} ions diffusion from the steel surface into molten corium is the corium crust on the steel specimen surface. Crust thickness is determined by solving the stationary heat conduction equation. Finally, experimental data have been generalized using the $W(T_{sol} - T_S)/q$ complex as a $1000/T_S$ function, where W is the corrosion rate, m/s; q is the heat flux, MW/m^2; T_{sol}, T_S are the corium solidus temperature and the steel surface temperature, respectively, K.

Fig. 3.1 generalizes the data from MCP-4 on the European reactor vessel steel corrosion in the indicated coordinates (the point designated as “final” does not refer to 6 tested regimes and is commented below). It is apparent that the points related to different corium compositions may be generalized by close correlations, or even by one correlation, that is, no apparent dependence of the corrosion rate on corium composition is observed, unlike in the case with the VVER vessel steel. Besides, there is no apparent and clear corrosion intensification (an abrupt increase of the rate) in the case with fusible corium when T_S of some value has been exceeded (for the VVER vessel steel, it was ~1050°C) [1]. A high rate of corrosion under these conditions is determined by the liquid phase diffusion of Fe^{2+} through the corium crust [1]. However, we believe that the mentioned differences are explained more by a limited number of experimental points in MCP-4 rather than by the influence of steel composition. It should be reminded that it took 6 tests with the VVER vessel steel in order to accumulate an array of experimental data.

For a comparison, Fig. 3.2 shows the points from MCP-4 along with the points referring to the VVER vessel steel. Obviously, all the points can be more or less satisfactorily generalized by the previously obtained correlations. The maximum deviation is observed for a point belonging to regime 6, that is, to the regime involving fusible corium and the maximum specimen surface temperature. Note, that the same effect is observed under similar conditions for the VVER vessel steel (MC11, regime 4, [3]). Presumably, it relates to the growing error of calculating the effective temperature that determines the rate of corrosion for the fusible corium under conditions of rapid processes at high temperatures on the interaction interface.

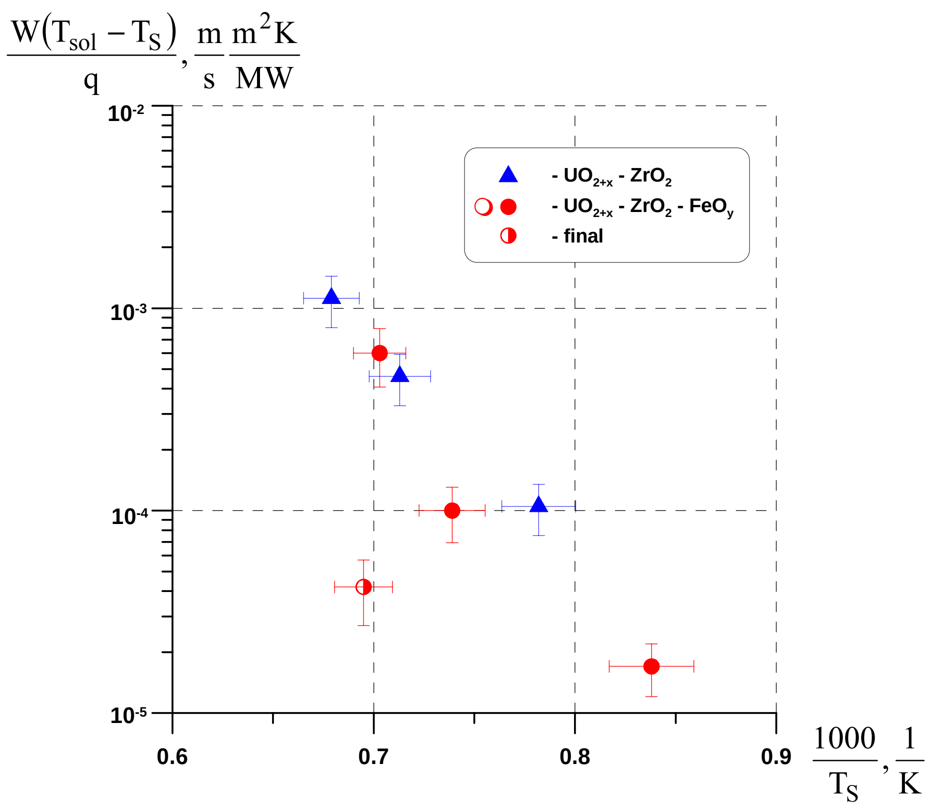

Fig. 3.1 – Generalization of data from MCP-4

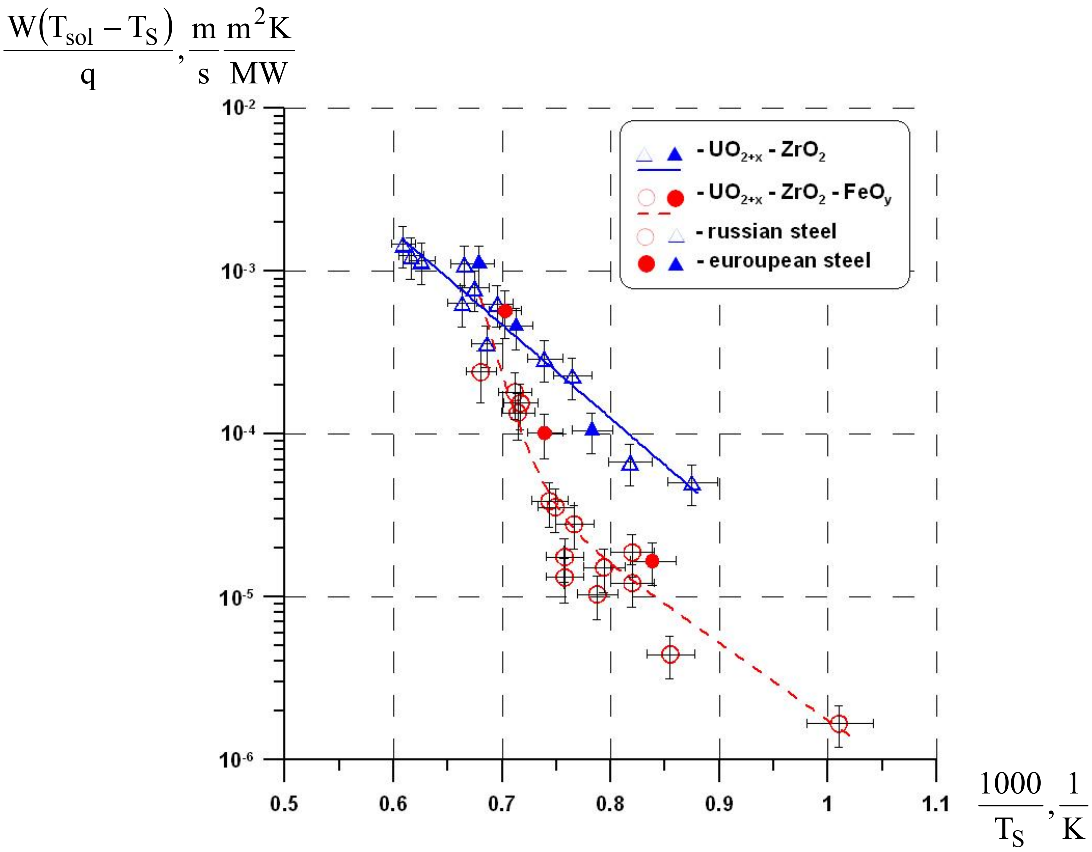

Fig. 3.2 – Generalization of data on corrosion of the Russian and European reactor vessel steel

In addition to those 6 regimes, the data on which are presented in Tab. 2.2 and Fig. 3.1, 3.2, let us consider the final stage of MCP-4 that lasted from the end of regime 6 till the inductor switching off, approximately from 31000 through 31800 s. The specimen temperature condition is close to that in the end of regime 6. However, the corrosion rate has dropped sharply (see Fig. 1.11) and amounted to just $0.23 \cdot 10^{-6}$ m/s. Fig. 3.3 shows the results of calculated specimen temperature condition during said regime in comparison with temperature changes. The temperature of the specimen surface central part was 1165ºC and the heat flux to it was 0.97 MW/m^2. The corresponding point has been plotted in Fig. 3.1. It is obviously located much lower than even the point from regime 5, in the latter regime the specimen surface temperature was 85ºC lower.

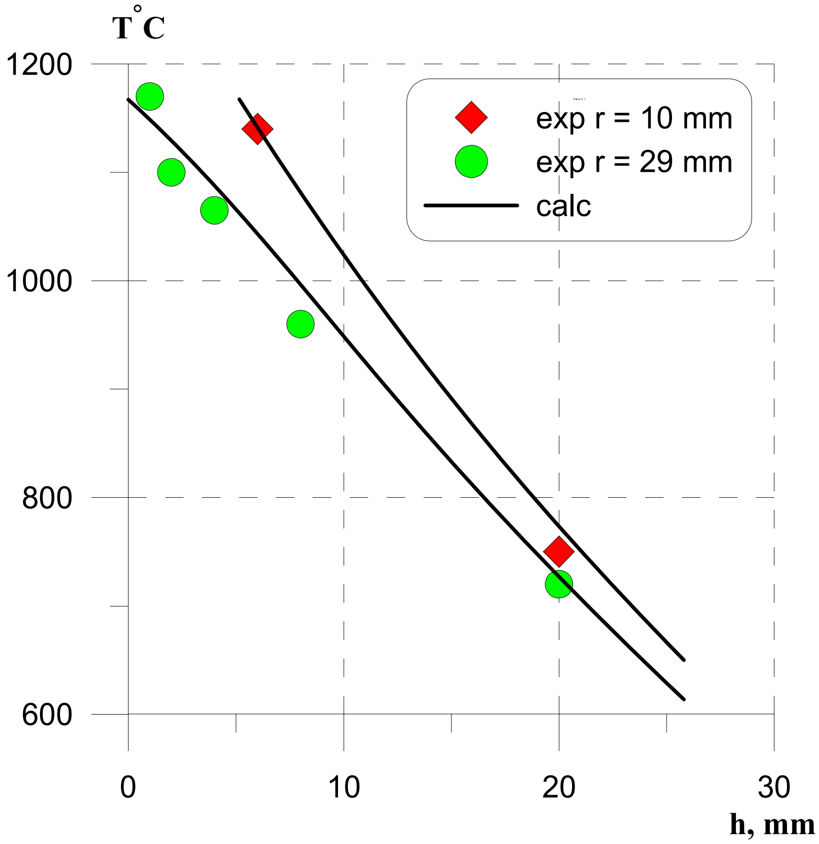

Fig. 3.3 – Temperature distribution in the specimen at the MCP-4 final stage

In search for a possible explanation of the described deviation, let us consider the measured oxygen concentrations in the evacuated gases (O_{x1}) throughout MCP-4, which are presented in Fig. 3.4 (smoothened in comparison with Fig. 1.9). It is necessary to note the unaccounted lag of “gas” measurements due to the transport lag in the pipeline and to inertia (capacity) of the furnace gas volume. The same figure shows the plotted data characterizing Fe^{3+} and U^{6+} fractions variation during the test depending on the content of $Fe^{2+} + Fe^{3+}$ and $U^{4+} + U^{6+}$, respectively, in the melt. These data were obtained from chemical analysis of melt samples (see Tab. 2.6).

A sharp drop in oxygen concentration in the evacuated gases, i.e., oxygen absorption by the melt after the addition of iron into it (for changing its composition) is clearly seen starting from approximately 15000 s. The reason is the disturbance of equilibrium (oxygen-wise) between the furnace atmosphere and the melt as a result of oxidation of the introduced iron. The melt oxygen potential also reduces (as the U^{6+} fraction decreases). The same effect, however, was observed starting from approximately from 30000 s, i.e., during regime 6. Obviously, it is connected with the high rate of steel specimen oxidation at a high temperature on its surface. It means that the oxygen spent on steel oxidation is not compensated by the oxygen coming from the atmosphere. The most representative data on the melt oxygen potential in the end of regime 6 are those obtained from the chemical analysis of the ingot average sample (shown at ~ 32500 s in Fig. 3.4). The fractions of U^{6+} and especially of Fe^{3+} in this sample are the minimal for the entire test. The data on sample 5 taken immediately after the end of regime 6 are less representative, since they reflect the local melt composition which may significantly differ from the average one after the rapid regime 6. It should be reminded that the model used for generalizing the experimental data neglects the resistance between the atmosphere and melt, and of the melt itself, to oxygen diffusion. It means that the effect of the changing oxygen potential of the melt in comparison with the conditions of equilibrium with the atmosphere is disregarded. Therefore, the process of Fe^{2+} (instead of O^{2-}) ions diffusion through the crust is regarded as the process that limits corrosion. However, it is obvious that when the melt oxygen potential is decreasing, the diffusion flow of O^{2-} ions also decreases, and when the oxygen potential reaches a certain value, it starts influencing the rate of corrosion and slows it down.

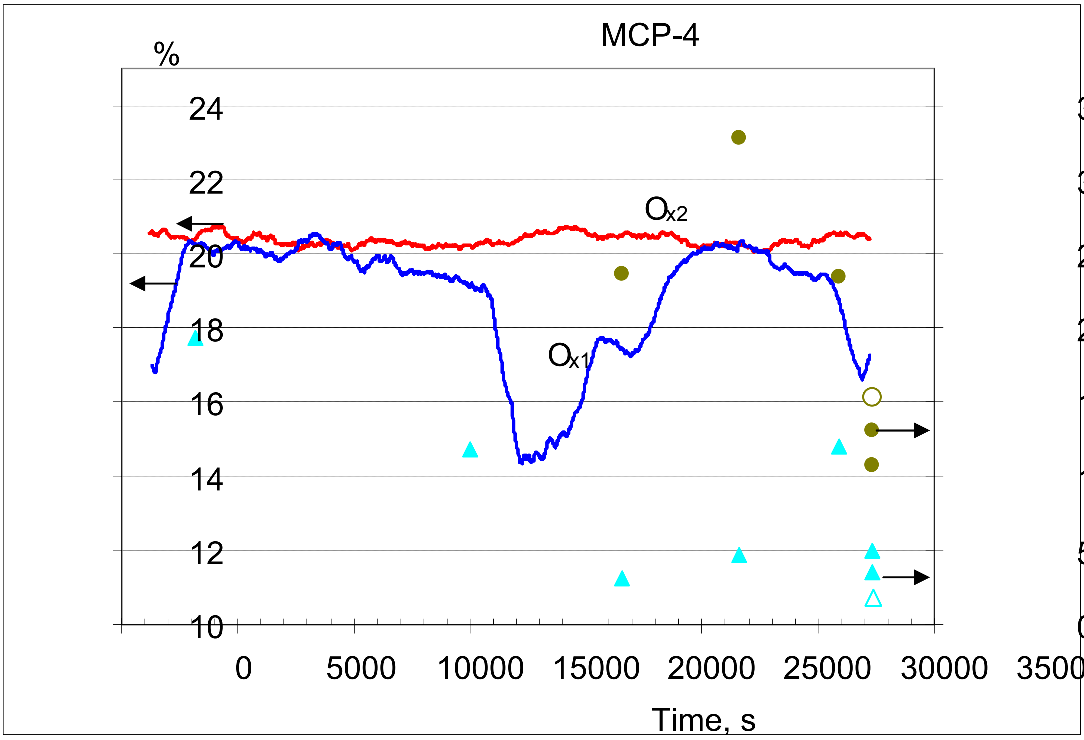

●, ○ – $Fe^{3+}/(Fe^{2+} + Fe^{3+})$; ▲, △ – $U^{6+}/(U^{4+} + U^{6+})$; △ , ○ – MC11

Fig. 3.4 – Oxygen concentration in the evacuated gases, and Fe^{3+} and U^{6+} fractions depending on $Fe^{2+} + Fe^{3+}$ and $U^{4+} + U^{6+}$, respectively, in the melt and ingot

Therefore, the described effect can be explained by the low oxygen potential of the melt by the end of regime 6. The oxygen potential value can be appreciated from the Fe^{3+} fraction in the ingot, which is noticeably smaller that during regime 5 according to Fig. 3.4.

The final stage of MC11 has been analyzed in a similar way. The rate of corrosion was at its maximum during regime 4 and amounted to $2.2 \cdot 10^{-6}$ m/s, while the specimen surface temperature was the highest one for the test. During a short exposure between the end of said regime till the inductor shutdown, approximately from 14800 through 14900 s ([3], П2, Fig. 2.2, 2.8), corrosion rate dropped significantly and amounted to $0.75 \cdot 10^{-6}$ m/s. Fig. 3.5 (like Fig. 3.3) offers a comparison of calculated and experimental data for the final stage of the test. Their agreement observed in the figure was achieved at 1175ºC on the steel specimen surface and a heat flux of 1.24 MW/m^2. A corresponding point is shown in Fig. 3.6 together with all the points relating to the VVER vessel steel in the tests with fusible corium in a similar temperature domain. The point is obviously located much lower than the correlation that generalizes the previously obtained results. In MC11 (like in other tests on steel corrosion in the oxidizing above-melt atmosphere, with exception for MCP-4) the composition of the evacuated gases was not analyzed and no melt samples were taken during the test, therefore the value of melt oxygen potential at the final stage of the test can be estimated only on the basis of the ingot composition. The fractions of Fe^{3+} and U^{6+} ions of the total Fe and U ions were determined by chemical analysis and amounted to 15.1 and 1.5%, respectively, that is, they were close to the values obtained for the ingot from MCP-4 (in Fig. 3.4, these concentration values are conventionally shown at ~ 32500 s). Therefore, the deviation of the considered point from the correlation may be linked with the reduced melt oxygen potential similarly to MCP-4.

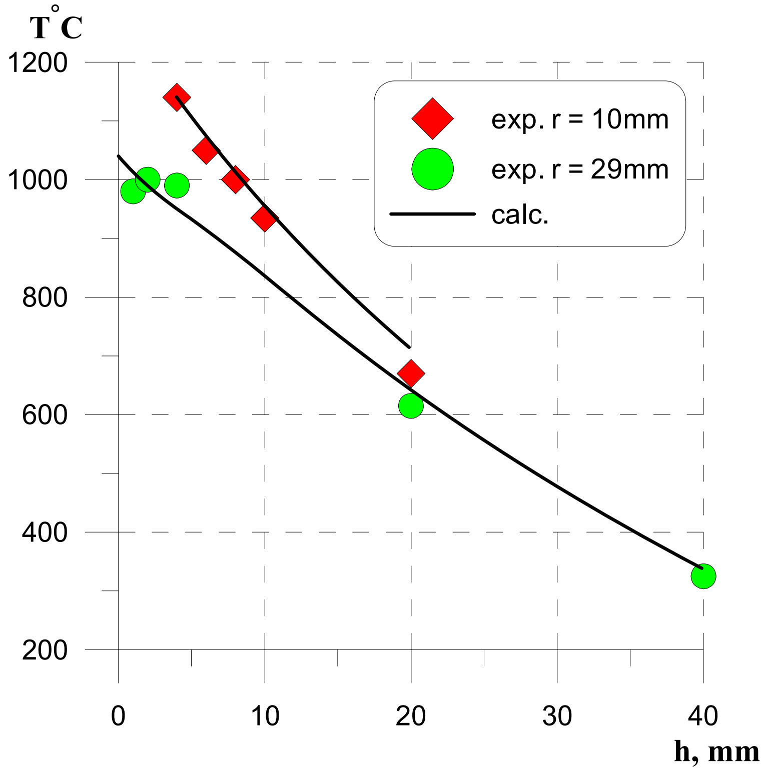

Fig. 3.5 – Temperature distribution in the specimen at the final stage of MC11

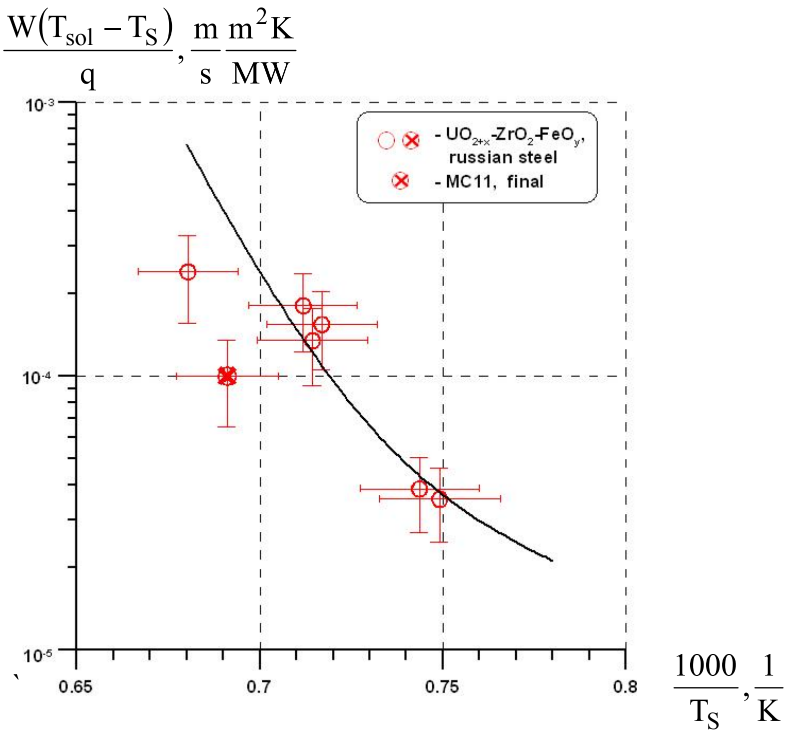

Fig. 3.6 – Generalization of data on corrosion of the VVER vessel steel at its interaction with fusible corium ($T_S \geq 1050$°C)

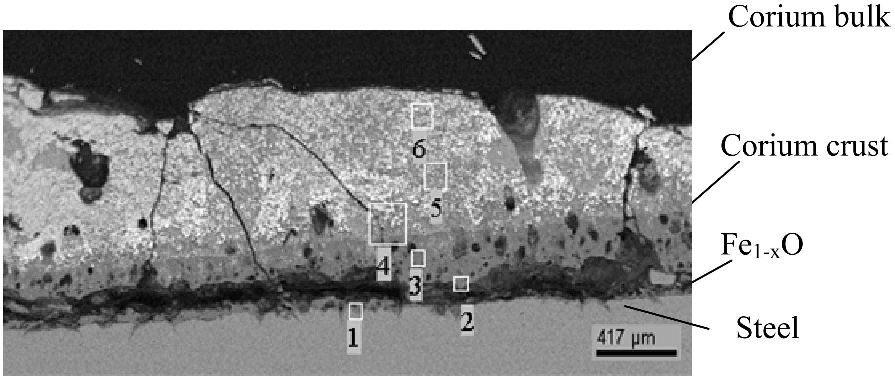

Fig. 3.7 – MC12. Corrosion layer and corium crust on the steel specimen surface

In order to understand how the melt oxygen potential influences the corrosion rate, let us compare the results of SEM/EDX analysis of the corrosion layer and the surface corium crust from MC12 and MCP-4. Please, be reminded that in MC12 the heating was switched off (with crystallization of molten fusible corium) during the regime of steel specimen intensive corrosion.

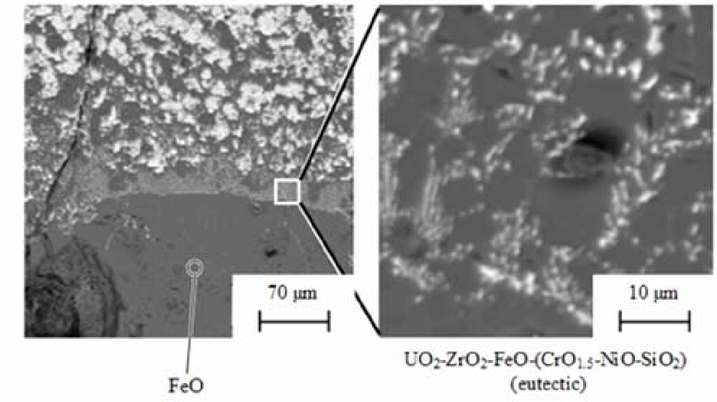

Fig. 3.8 – MC12. SEM image of the corrosion layer boundary and of the corium crust (zone 4 in Fig. 3.7)

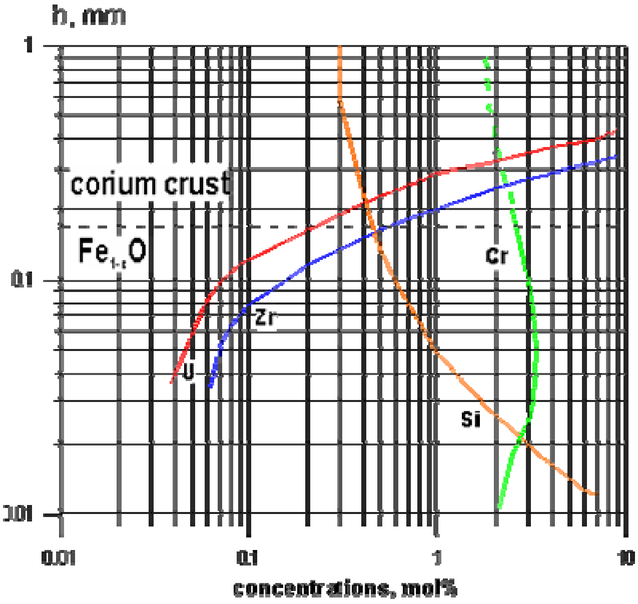

Fig. 3.9 – MC12. Distribution of corium and steel components along the height (from steel surface to the melt)

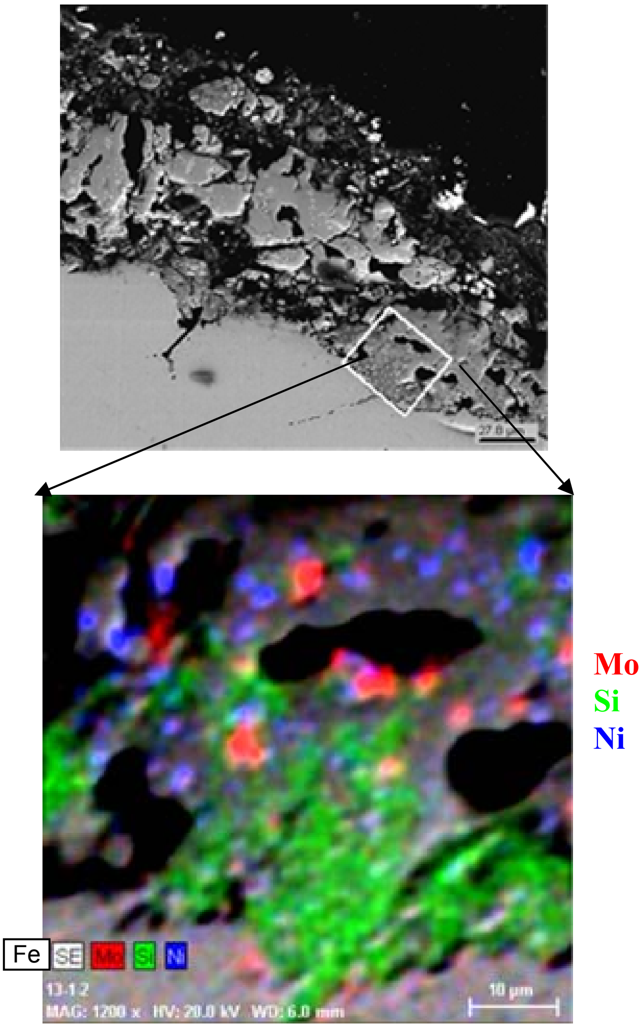

Fig. 3.10 – MCP-4. SEM image of the corrosion layer

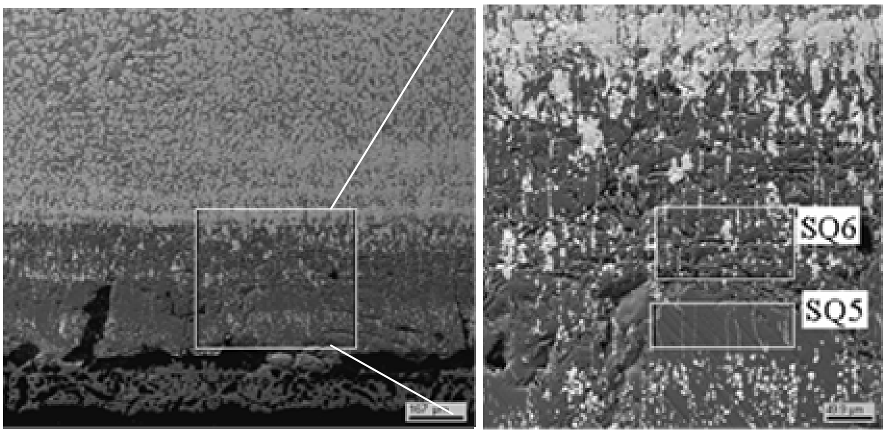

Fig. 3.11 – MCP-4. SEM images of the corrosion layer boundary and of the corium crust

Table 3.1 – EDX analysis data (re. Fig. 3.11)

Region		U	Zr	Fe	Mn	Ni	O
SQ5	mass %	2.2	2.4	66.7	1.1	0.6	27.0
	mol. %	0.3	0.9	40.5	0.7	0.3	57.3
	mol. % MeO_x	0.8	2.1	94.8	1.5	0.8	
SQ6	mass %	10.5	4.0	53.6	0.6	0.7	30.6
	mol. %	1.5	1.5	32.1	0.4	0.4	64.2
	mol. % MeO_x	4.1	4.1	89.6	1.1	1.1	

A conclusion about the development of liquid phase diffusion of steel and corium ions leading to an intensified corrosion of steel at its interaction with molten fusible corium after the interface temperature has surpassed 1050ºC was based in [1] on the results of SEM/EDX presented in Figs. 3.7, 3.8. The figures show a layer of eutectic liquid at the corrosion layer/corium crust boundary. This liquid was found to penetrate the corium crust. The formation of a low-temperature eutectic was explained in [1] by the compounds containing Si that transits into the corrosion layer and further the melt from steel. It may be seen from Fig. 3.9 that the concentration of Si is at its maximum at the steel surface, that it decreases away from the surface, but remains noticeable within the corium crust.

The SEM/EDX results for MCP-4 look differently. Fig. 3.10 confirms that the concentration of Si in the corrosion layer at the steel surface seems to be sufficiently high, like in MC12. However, it follows from Fig. 3.11 and Tab. 3.1 that neither Si nor liquid phase were observed at least starting from the corrosion layer boundary and further towards the melt.

Fig. 3.12 offers a comparison of characteristic microstructures of the zones enriched in iron oxide, and of the boundaries of these zones with corium in MC12 and MCP-4, which confirm the presence of a liquid phase in MC12 and the absence of a liquid phase in MCP-4. For instance, the intergrain area width in MC12 is much bigger than in MCP-4 and it contains dome corium components which were missing in the similar area in MCP-4.

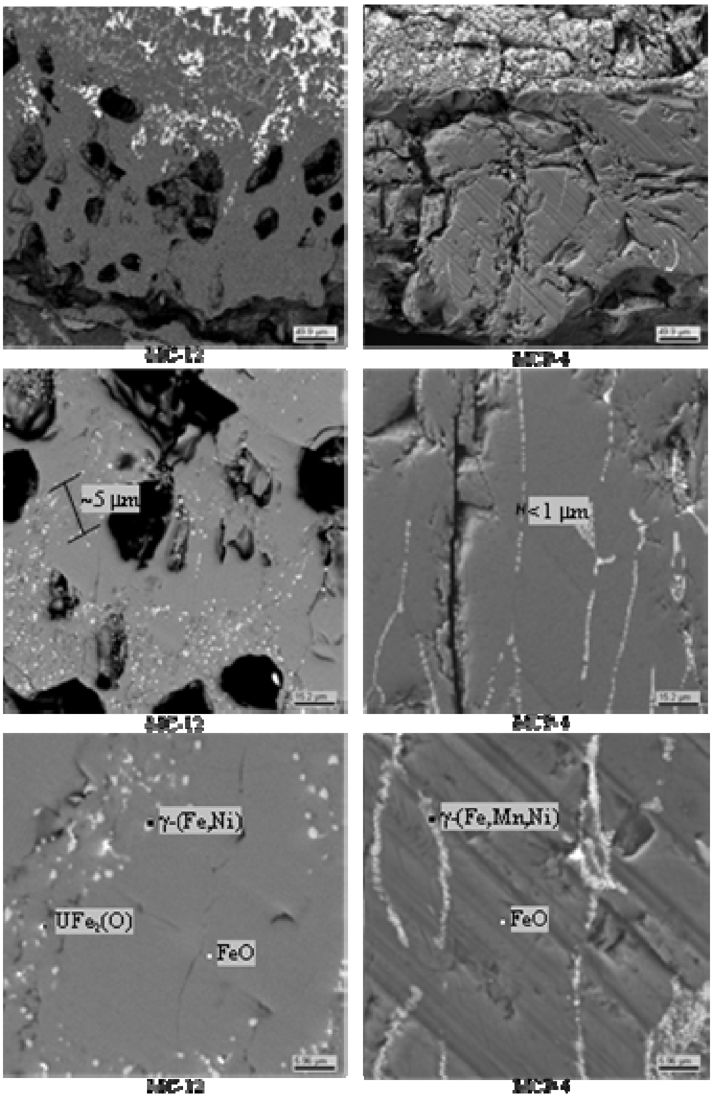

Fig. 3.12 – A comparison of the corrosion layer microstructure in MC12 and MCP-4

Fig. 3.13, like Fig. 3.2, presents the data for the VVER steel (only for the fusible corium and for a surface temperature below 1050ºC), as well as said data for the final stage of MCP-4 and MC11. While the generalizing correlation for the fusible corium in Fig. 3.2 looks like

$$\frac{W(1613-T_S)}{q}=0.1\exp\left(-\frac{0.91\cdot10^5}{RT_S}\right)+3.4\cdot10^{14}\exp\left(-\frac{4.99\cdot10^5}{RT_S}\right),$$

The analogous correlation in Fig. 3.12 has the following appearance:

$\frac{W(1613-T_S)}{q}=0.1\exp\left(-\frac{0.91\cdot10^5}{RT_S}\right)$, that is, the data obtained when the melt oxygen potential is low, can be generalized by a correlation that reflects only the solid phase diffusion of Fe ions [1].

Therefore, the obtained results allow a supposition that the effect of corrosion rate reduction along with the decreasing melt oxygen potential reveals itself only (or mainly) in the limitation of development of the liquid phase diffusion through the oxidic corium crust on the steel surface.

The noted influence of the melt oxygen potential on the corrosion rate requires a purposeful experimental investigation, on the one hand, while on the other hand, it should be taken into consideration when evaluating corrosion of vessel steel, in particular, in view of the possibility of its liquid phase burning under IVR conditions discussed in [3]. The measured oxygen concentrations in the evacuated gases in MCP-4 together with the data on the oxygen concentration in the melt obtained by chemical analysis of melt samples and the ingot have shown that a strong sensitivity of the melt oxygen potential to the corrosion rate is characteristic of METCOR tests. Therefore, it will be possible to model the liquid phase burning in medium-scale tests on experimental facilities of the Rasplav platform only after a significant redesigning of the furnace and specimen, or/and a considerable change of the conditions of the oxidizing atmosphere supply to the melt surface. It should be noted that in real IVR conditions, the big mass of the melt (oxygen reserve) and the wide area of the surface contacting with the atmosphere may damp the influence of the intensifying corrosion on the melt oxygen potential.

For the conditions of VVER-1000 and METCOR tests, Fig. 3.14 schematically shows the parameters (and their values) which influence the oxygen potential of the melt during its interaction with the vessel leading to the vessel steel corrosion.

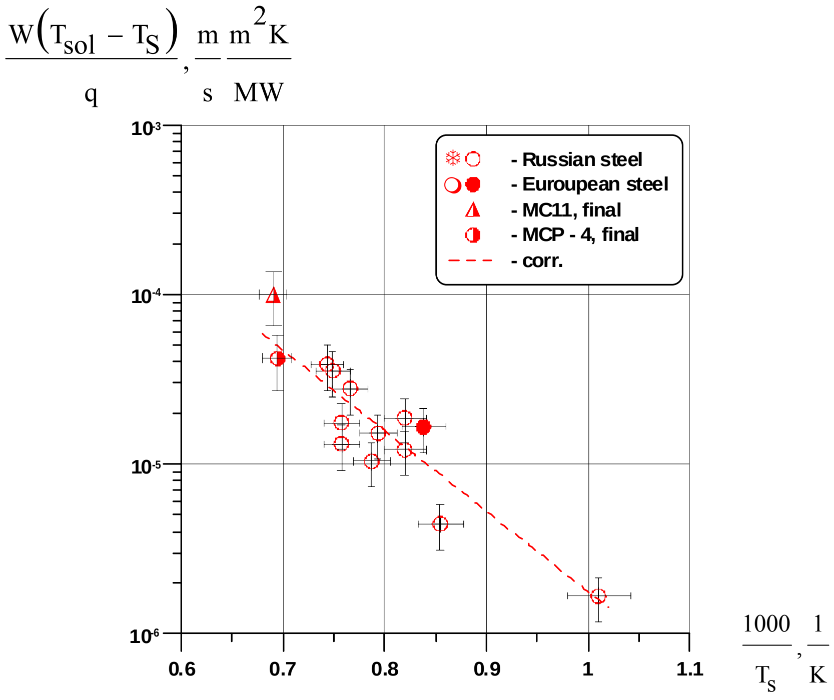

Fig. 3.13 – Generalization of data on the corrosion of vessel steel at its interaction with fusible corium under conditions of solid phase diffusion

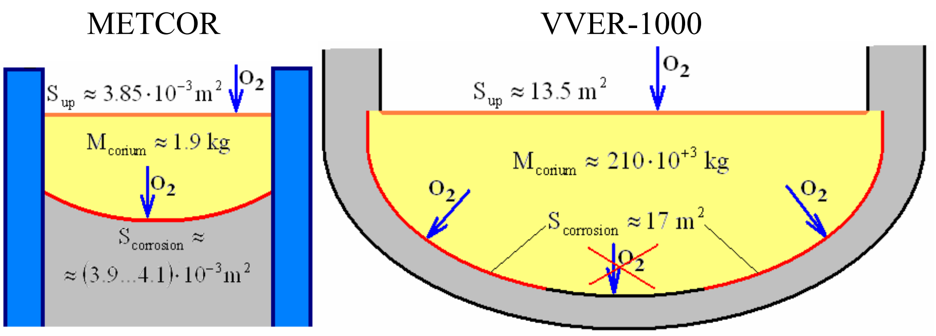

Fig. 3.14 – Conditions determining oxygen balance in the molten pool

Time variation of the melt oxygen potential (oxygen concentration) as a result of steel corrosion has the following appearance:

$$\frac{dC_{O2}}{dt} = \frac{1}{M_{corium}}\left(G_{O2}S_{up} - kW_{corrosion}S_{corrosion}\right);$$

where C_{O2} is the oxygen concentration in the melt,

M_{corium} is the mass of the melt, kg,

$W_{corrosion}$ is the rate of corrosion, m/s,

$k = \rho_{Fe}\ \mu_O/\mu_{Fe}$, kg/m^3,

ρ_{Fe} is the density Fe, kg/m^3,

μ_O, μ_{Fe} –is the atomic weight of O and Fe, respectively, kg/кmol.

During intensive steel oxidation when the oxygen spent on oxidation is not compensated by that entering the melt through the pool surface, the below inequality is true in the limit

$$\left|G_{O_2}S_{up}\right| << \left|\ kW_{corrosion}S_{corrosion}\right| \ .$$

Then, the ratio between the rates of melt oxygen potential reduction during corrosion can be determined for equal corrosion rates under the conditions of VVER-1000 and METCOR tests

$$\left(\frac{dC_{O2}}{dt}\right)_{VVER} \Big/ \left(\frac{dC_{O2}}{dt}\right)_{METCOR} \approx \left(\frac{M_{corium}}{S_{corrosion}}\right)_{METCOR} \left(\frac{S_{corrosioon}}{M_{corrium}}\right)_{VVER} \approx 0.05$$

Thus, the melt oxygen potential under the VVER-1000 conditions is about 20 times less sensitive to oxygen consumption for steel oxidation than in METCOR tests.

In general, a comparison of the results of MCP-4 with those of the previously performed tests allow a conclusion that the differences in corrosion of the European and VVER vessel steels are insignificant when the melt oxygen potential is high (close to an equilibrium with the atmosphere). It means that the correlations suggested in [1, 2] are applicable to said conditions. This conclusion could be substantiated even more by a bigger array of experimental data on the European reactor vessel steel.

The final note is as follows: it has been demonstrated in [19] that the vessel steel corrosion has no effect on the vessel strength under IVR conditions, nevertheless, it may be important to take it into consideration 1) when assessing DNB margin for the vessel outer surface, if the regime of liquid phase burning [3] will turn out to be realizable, and 2) for evaluating the additional generation of hydrogen as a result of absorption of oxygen from steam by the melt to compensate the oxygen spent on steel oxidation.

CONCLUSIONS

The test performed to investigate the interaction of molten prototypic corium with the cooled specimen of the European reactor vessel steel in air above the melt has shown that

- The limited volume of the obtained experimental data is insufficient for their generalization. An evaluation of the corrosion rate for the European reactor vessel steel may rely on the correlations obtained for the VVER vessel steel.
- The rate of corrosion slows down as the melt oxygen potential decreases. Under conditions of the test, it was registered at the interaction of steel with molten fusible corium containing iron oxides, at >1150°C on the steel surface.

Quantitative characteristics of the corrosion rate during oxidation with the oxidized corium are similar for the Russian and European vessel steels when the melt oxygen potential is high but depend on its value in general. This circumstance and the factors influencing the melt oxygen potential should be taken into account when evaluating vessel steel corrosion under IVR conditions.

REFERENCES

1. S.V. Bechta, V.S. Granovsky, V.B. Khabensky, et al., “Interaction between Molten Corium UO_{2+x}–ZrO_2–FeO_y and VVER Vessel Steel”, *Proc. of ICAPP’08*, Paper 8052, Anaheim, CA USA, June 8-12, 2008.
2. S.V. Bechta, V.S. Granovsky, V.B. Khabensky, et al., “VVER Vessel Steel Corrosion of Interaction with Molten Corium in Oxidizing Atmosphere”, *Nucl. Eng. Design*, 239 (2009), pp. 1103-1112.
3. Investigation of corium melt interaction with NPP reactor vessel steel (METCOR). ISTC Project No. 833.2-2003. Final Technical Report (2006).
4. Markov V. K. et al. Uranium. Methods of its determination. Moscow, Atomizdat Publishers, 1964. (in Russian)
5. Riabchikov D.I., Seniavin M.M. Analytical chemistry of uranium. Moscow, Publishing House of the USSR Academy of Sciences. 1962. (in Russian)
6. Lukianov V.F., Savvin S.B., Nikolskaya I.V. Photometric detection of uranium microquantities using reagent arsenazo III. JACh., v. XV, issue 3. 1960. (in Russian)
7. GOST 12365-84. Alloy and high-alloy steels. Methods of zirconium determination. (in Russian).
8. Yelinson S.V., Nezhnova T.I. Photometric determination of zirconium in niobium and other metals // Factory laboratory. Vol. 30, No.4, 1964.p. 396-399. (in Russian).
9. Goryushina V.G., Romanova E.V., Archakova T.A. Colorimetric methods of zirconium determination in alloys // Factory laboratory. Vol. 27, No.7, 1961. p. 795-797. (in Russian).
10. GOST 4011-72. Drinking water. Methods for determination of total iron. (in Russian).
11. Sendel E. Methods of metal traces determination by colorimetry. Moscow, Mir Publishers, 1964. (in Russian).
12. Bekkert M, Klemm H. Reference book on metallographic etching. (transl. from German), Moscow, Metallurgiya Publishers, 1988. (in Russian).
13. G. Tamman, “Uber Anlauffarben von Metallen”, Z. anorg. Allg, Chem. B., 111. H 1.5, 78-89 (1920)
14. KOYAMA K.; HARADA T. Phase diagram of Fe-Mo-O system at 1173 -1473 K //Nippon Kinzoku Gakkaishi. 1994, vol. 58, N 12, pp. 1401-1407.
15. Almjashev V.I., Barrachin M., Bechta S.V. et al. Phase equilibria in the FeO_{1+x}–UO_2–ZrO_2 system in the FeO_{1+x}-rich domain // JNM. 2010. V. 400. N. 2. P. 119–126.
16. Almjashev V.I., Barrachin M., Bechta S.V. et al. Eutectic crystallization in the $FeO_{1.5}$–UO_{2+x}–ZrO_2 system // JNM. 2009. V. 389. N. 1. P. 52–56.
17. Thermochenical Equilibria Calculation Code GEMINI2. Version 3.4. Gibbs Energy MINImizer. Copyright©THERMODATA 2003, Saint Martin d’Heres, France.
18. Nuclear Thermodynamic Database “NUCLEA”. Version iv-10.1, Copyright©THERMODATA 2010, Saint Martin d’Heres, France.
19. S.V. Bechta, V.B. Khabensky, E.V., Krushinov et al., VVR steel corrosion during in-vessel retention of corium melt, Pros. ERMSAR-2008, Bulgaria, 2008.